Mid-infrared photodetection with 2D metal halide perovskites at ambient temperature

Yanyan Li[1,2], Shunran Li[1,2], Du Chen[1,2], Conrad A. Kocoj[1,2], Ankun Yang[3], Benjamin T. Diroll[4], Peijun Guo[1,2,]*

[1]Department of Chemical and Environmental Engineering, Yale University, 9 Hillhouse Avenue, New Haven, CT 06520, USA

[2]Energy Sciences Institute, Yale University, 810 West Campus Drive, West Haven, CT 06516, USA

[3]Department of Mechanical Engineering, Oakland University, Rochester, MI 48309, USA

[4]Center for Nanoscale Materials, Argonne National Laboratory, 9700 South Cass Avenue, Lemont, IL 60439, USA

Abstract

The detection of mid-infrared (MIR) light is technologically important for applications such as night vision, imaging, sensing, and thermal metrology. Traditional MIR photodetectors either require cryogenic cooling or possess sophisticated device structures involving complex nanofabrication. Here, we conceive spectrally tunable MIR detection by using two-dimensional metal halide perovskites (2D-MHPs) as the critical building block. Leveraging the ultralow cross-plane thermal conductivity and strong temperature-dependent excitonic resonances of 2D-MHPs, we demonstrate ambient temperature, all-optical detection of MIR light with sensitivity down to 1 $nW \cdot \mu m^{-2}$, employing plastic substrates. Through the adoption of membrane-based structures and a photonic enhancement strategy unique to our all-optical detection modality, we further improved the sensitivity to sub-10 $pW \cdot \mu m^{-2}$ levels. The detection covers the mid-wave infrared regime from 2 to 4.5 microns and extends to the long-wave infrared wavelength at 10.6 microns. Our work opens a pathway to new types of solution-processable, long-wavelength thermal detectors for molecular sensing, environmental monitoring, and thermal imaging.

INTRODUCTION

The mid-infrared (MIR) spectral range, encompassing both mid-wave (MWIR, 3~5 μm) and long-wave (LWIR, 8~14 μm) infrared regions, is pivotal in numerous technological fields including gas and molecular sensing,[1,2] bio-imaging,[3] environmental monitoring,[4] free-space communication,[5] and thermal energy harvesting.[6] However, in stark contrast to the detection of visible and near-infrared light, MIR light detection presents unique challenges due to the inherently low photon energies involved. Traditional MIR photon detectors constructed from narrow-bandgap semiconductors, such as PbS, InSb, and HgCdTe, require cryogenic cooling to function effectively, which leads to increased size, weight, cost, and likelihood of device failure.[7,8] The spectral responsivity of these detectors is constrained by the electronic bandgap of light-absorbing semiconductors. On the other hand, MIR thermal detectors, also known as bolometers, can operate at ambient temperature over a broader spectral range, at the expense of reduced detection bandwidth.[9] Bolometers typically consist of a MIR light-absorbing element in close proximity to a temperature-sensitive resistive material, such as vanadium oxide (VO_x with x ranging from 1.8 to 2) and amorphous silicon. To minimize thermal conductance between the heat-sensitive element and the support substrate, these detectors often incorporate complex device architectures that require multiple lithographic steps.[10]

In recent years, several innovative approaches for MIR detection have emerged. For instance, a nanoparticle-on-resonator-based scheme was reported to convert 10-μm-wavelength light into visible light by leveraging strong interactions between molecular vibrational modes and plasmonic near-fields, achieving a sensitivity of 1 $\mu W \cdot \mu m^{-2}$.[11] Another approach, which employed lanthanide-based $NaYF_4$:Nd@$NaYF_4$ core-shell nanotransducers, exploits ratiometric luminescent properties to detect infrared radiation in the 4.5 to 10.8 μm range, with a detection limit of ~ 0.3 $nW \cdot \mu m^{-2}$.[12] Additionally, 1T-TaS_2, a charge-density-wave material, has been shown for light detection from visible to terahertz wavelengths, with responsivities up to 300 $pW \cdot Hz^{-1/2}$.[13] A further approach used plasmonic antennas coupled with hyperbolic phonon polaritons in hexagonal boron nitride (*h*-BN) to funnel MIR light onto a graphene pn-junction, enabling resonant detection in the 6.2 to 7.3 μm range, with a sensitivity of 82 $pW \cdot Hz^{-1/2}$.[14] In another report, a $PtTe_2$/Si Schottky junction-based photodetector, built on a mosaic-like 2D $PtTe_2$ layer with ultrawide light absorption, has demonstrated light detection across a broad range from 0.2 to 10.6 μm.[15] Despite these advancements, the quest for new materials and detection concepts that can improve speed and device scalability, while reducing fabrication costs, remains a high priority for MIR detection.

RESULTS

2D perovskites for MIR detection

Metal halide perovskites (MHPs) have emerged as solution-processable semiconductors with promising applications in photovoltaics and optoelectronics.[16-22] The strong electron-phonon interactions in MHPs lead to temperature-dependent variations in photoluminescence linewidths[23-25] and facilitate the formation of polarons, which dominate trapping, transport, and recombination of charge carriers in these materials.[26,27] Two-dimensional (2D) MHPs represent a structurally and

chemically diverse sub-class of the MHP family with favorable optoelectronic properties.[28-30] The charge-insulating organic-spacer cations in 2D-MHPs not only impose dielectric and quantum confinements on charge carriers,[31-33] leading to the formation of excitons with spectrally narrow and strong optical absorption at room temperature, but also strongly impede heat flow along the cross-plane direction.[34-36]

While their ultralow thermal conductivity (denoted as κ) is unfavorable for 2D-MHPs in optoelectronic applications, here, we take advantage of this property as well as the strong temperature dependence of exciton-lattice interactions for a previously uncharted application of 2D-MHPs in thermal-type MIR photodetection. Our work demonstrates the viability of using 2D-MHPs as a novel and unique material platform for scalable, cost-effective MIR photodetection applications. **Fig. 1a** shows the temperature-dependent reflectance spectra of $(PEA)_2PbI_4$ (abbreviated as PEA throughout this manuscript) single crystals, where $PEA^+ = C_6H_5C_2H_4NH_3^+$, the phenylethylamine cation. $(PEA)_2PbI_4$ was chosen in this work due to this facile solution processability to yield high-crystallinity films and single-crystal membranes.[37] The spectra were measured with unpolarized light at normal incidence on the crystalline *a-b* plane or the (001) plane, which is parallel to the octahedral layers. The exciton resonance is manifested as a peak in reflectance near 520 nm and a dip on the shorter-wavelength side. Such a spectral feature in reflectance can be quantitatively captured by modeling the exciton resonance using a Lorentzian oscillator, with which the relative permittivity at angular frequency ω is written as $\varepsilon(\omega) = \varepsilon_\infty + \frac{{A_\mathrm{L}}^2}{{\omega_\mathrm{L}}^2-\omega^2-i\omega\gamma}$.[38-40] By fitting the reflectance spectrum at room temperature, we obtained the high-frequency permittivity $\varepsilon_\infty = 5.07$, oscillator strength $A_\mathrm{L} = 1.15\ \mathrm{eV}$, exciton energy $\omega_\mathrm{L} = 2.39\ \mathrm{eV}$, and damping factor $\gamma = 67\ \mathrm{meV}$ (Fig. S1).

As shown in **Fig. 1a**, the resonant feature in reflectance strengthens with decreasing temperature, which results in a further increase (decrease) of reflectance at the reflectance peak (dip).[41,42] This trend arises from reduced electron-phonon interactions at lower temperatures, leading to homogeneous exciton linewidth-narrowing. Notably, the low reflection value at the reflectance dip (500~510 nm) and its spectral shift with temperature yield a large temperature coefficient of reflectance (TCR), defined as the relative change in reflectance per degree change in temperature: $\mathrm{TCR}(T) = \frac{R(T+dT)-R(T)}{R(T)\cdot dT}$, where T is temperature and R is the temperature-dependent reflectance. As shown in **Fig. 1b**, at ambient temperature, the TCR is $0.52\%\cdot K^{-1}$, which goes up to $2\%\cdot K^{-1}$ at liquid-nitrogen temperature. The wavelength of maximal TCR slightly varies with temperature due to the spectral shift of the reflectance dip (Fig. S2).

Similar to other *n*=1 2D-MHPs,[30] spin-coated PEA films exhibit a high degree of out-of-plane alignment (*i.e.*, *a-b* planes parallel to substrates), as verified with X-ray diffraction (XRD; Fig. S3). **Fig. 1c** shows the temperature-dependent reflectance spectra for a 1.0 μm-thick spin-coated PEA film. Since the thickness is larger than the optical penetration depth around the exciton resonance (Fig. S1d), the film is considered infinitely thick, and the reflectance is substrate-blind. The film exhibits a TCR of approximately $0.3\%\cdot K^{-1}$ at ambient temperature (**Fig. 1b**). The lower

TCR of the film, as well as the slightly different temperature dependence of the exciton resonance, compared to its single-crystal analogue likely arises from disordered in-plane crystallographic orientations,[43] strain imposed by the substrate, and defects, which yield additional exciton damping pathways as evident from the broadened resonance in the reflectance spectra (**Fig. 1c**). The sizeable exciton-enabled TCR of PEA single crystals and films offers an opportunity for all-optical MIR photodetection, where the MIR light-induced temperature rise of PEA is detected by measuring the relative change in reflectance at the reflectance dip where the TCR is at its maximum.

Strong light-induced temperature effects are favored for the proposed MIR detection and is generally observed in materials with low κ. Due to the high density of organic-inorganic interfaces and the weak van der Waals forces connecting the organic cations between neighboring layers,[34] 2D-MHPs have some of the lowest κ among extended solids, especially along the cross-plane direction. To determine the cross-plane κ of PEA at ambient temperature, we performed infrared-pump visible-probe (IPVP) transient reflection (TR) experiments for a 640 nm-thick PEA film deposited on single-crystalline Si wafer. The PEA was vibrationally (*i.e.*, thermally) excited by MIR pulses centered at 3170 nm (resonant with the N-H and C-H stretching modes), and the pump-induced reflectance change was captured by a time-delayed, broadband visible probe.[44] Since the pump photon energy is much lower than the electronic bandgap, the relevant process is a solely pump-induced, impulsive lattice heating, followed by its subsequent dissipation. The measured $\Delta R/R$ transient spectral map is shown in Fig. S4, where $\Delta R/R = [R(t) - R(0)]/R(0)$ is the differential change in reflectance with $R(0)$ being the reflectance prior to pump excitation and $R(t)$ the reflectance at delay time t after pump excitation. The $\Delta R/R$ spectra exhibit a derivative-like line shape, transitioning from positive to negative at a zero-crossing wavelength of approximately 507 nm. The $\Delta R/R$ spectra, when compared with the steady-state data (Figs. 1a and 1c), indicate impulsive pump-induced lattice heating followed by slow cooling in the μs timescale. Since lattice cooling typically takes nanoseconds (*e.g.*, as measured in time-domain thermoreflectance),[45] the μs cooling time here reveals an ultralow cross-plane κ of PEA.

Using the finite-element method (see Materials and Methods section in Supplementary Materials), we simulated the heat transfer process in PEA/Si with PEA subject to impulsive thermal excitation. The initial temperature profile in PEA was determined by its absorption coefficient at the MIR pump wavelength. A linear relationship was assumed between the measured $\Delta R/R$ and the simulated temperature rise (denoted as ΔT, averaged over the probe's penetration depth). By sweeping the κ of PEA and the interfacial thermal conductance (G) between PEA and Si, we calculated the time-dependent ΔT, and with it the time-integrated differences between the decays of $\Delta R/R$ and ΔT. The obtained difference map (**Fig. 1d**) distills $\kappa = 0.20\ \mathrm{W \cdot m^{-1} \cdot K^{-1}}$ for PEA (assuming $G > 20\ \mathrm{MW \cdot m^{-2} \cdot K^{-1}}$). The sensitivity analysis in **Fig. 1e** indicates that the estimated κ of PEA should lie within ±20% of the true value.

Having determined the κ, we can then calculate the figure of merit, which we define as $\mathrm{TCR}/(\kappa \cdot C_p)$, to quantify material performance for bolometer applications. The figure of merit is defined as $\mathrm{TCR}/(\kappa \cdot C_p)$ since a higher TCR, a lower κ, and a lower C_p all contribute to improved

MIR light-induced material response. As presented in Table 1, PEA exhibits a figure-of-merit an order of magnitude higher than current state-of-the-art bolometer material VO_x.[46,47] The sizeable TCR and exceptional heat retention of 2D-MHPs motivated us to repurpose these materials for MIR photodetection.

Material	κ ($W \cdot m^{-1} \cdot K^{-1}$)	TCR ($\% \cdot K^{-1}$)	C_p ($J \cdot g^{-1} \cdot K^{-1}$)	Figure of merit
VO_x	3.5~6	2	0.65	5~9
PEA	0.20	0.52	0.46	57

Table 1. A comparison between the state-of-the-art bolometer material VO_x and PEA. The figure of merit is defined as $\mathrm{TCR}/(\kappa \cdot C_p)$ with a dimension of 10^{-6} $kg \cdot m \cdot s \cdot K^2$. R denotes resistivity for VO_x and reflectance for PEA. All properties are for room temperature.

Interfacing PEA with MIR-absorbing nanoantennas

To enable photodetection, we first employed plastic polyethylene terephthalate (PET) as the underlying substrate to enhance heat retention within the PEA film, leveraging the low κ of PET ($< 0.20\ \mathrm{W \cdot m^{-1} \cdot K^{-1}}$). The transient $\Delta R/R$ spectral map from IPVP experiments for a 940 nm-thick PEA film spin-coated on a PET substrate is shown in **Fig. 1f**. Importantly, the slow decay of $\Delta R/R$ takes tens of μs (*i.e.*, an order of magnitude longer than PEA/Si in **Fig. 1e**), suggesting effective heat retention within the PEA film. However, similar to VO_x, 2D-MHPs are transparent to MIR light except at discrete vibrational frequencies of the organic spacers. Strong MIR light absorbers need to be placed in proximity to 2D-MHPs, preferably away from the substrate, to enable the MIR detection functionality. To this end, localized surface plasmon resonances (LSPRs) provide a strong optical absorption cross-section with sub-wavelength material volumes. We harvest LSPRs of indium-doped cadmium oxide (ICO), a type of transparent conducting oxide (TCO) with low optical loss and tunable electron concentration.[48-50] Besides providing MIR absorption, another important advantage of TCOs is visible transparency, making them compatible with the all-optical detection scheme here.

We synthesized colloidal nanocrystals (NCs) of ICO with a high size-uniformity by established ramped heating methods.[51] By adjusting the dopant concentrations, three different NCs were prepared, and with a decreasing doping concentration, NCs dissolved in carbon tetrachloride exhibit LSPRs centered at 1.6, 2.4, and 3.4 μm (Fig. S5). Due to increased inter-particle interactions and higher dielectric constants of the surrounding medium, spin-casted NC films show redshifted LSPRs centered at 2.0, 3.0, and 4.4 μm (**Fig. 2a**); we denote these NCs as FICO (fluorine- and indium-doped cadmium oxide), ICO-1 (indium-doped cadmium oxide-1), and ICO-2, respectively. We spin-coated NC films onto the PEA/PET stacks. A 15-nm, visibly transparent Al_2O_3 layer was pre-evaporated on the PEA/PET to prevent PEA from damage by toluene, the solvent of the ICO NCs. **Fig. 2b** shows a cross-sectional scanning electron microscopy (SEM) image of the ICO-1/PEA/PET stack; the corresponding XRD pattern illustrates the structural integrity of the PEA film with NC deposition. MIR transmittance spectra of the three types of

ICO/PEA/PET samples are plotted in **Fig. 2c**. Notably, the absorption of MIR light by ICO NCs is largely preserved for the stacks, indicating the effectiveness of LSPR-enabled, spectrally tunable MIR absorption. Note that the LSPR absorption of ICO-1 overlaps with, but is much broader than, the N-H stretching absorption of PEA.

The transient $\Delta R/R$ spectral map (**Fig. 2d**) for the ICO-1/PEA/PET sample, pumped at 3170 nm, displays a similarly slow timescale as the PEA/PET (**Fig. 1f**). However, the $\Delta R/R$ of ICO-1/PEA/PET undergoes a slower rise (~100 ns) after time zero, whereas the $\Delta R/R$ of PEA/PET rises instantaneously following pump excitation (**Fig. 2e** and Fig. S6). Such disparity is also observed for samples on Si substrates (Fig. S7). Due to the visible transparency of ICO, the $\Delta R/R$ at 500 nm primarily arises from the temperature increase of PEA, hence the 100-ns rise of $\Delta R/R$ can be ascribed to the NC-to-PEA heat transfer (Fig. S8). Given a lack of knowledge on the κ for the NC film, we used several different κ for the NC film to simulate heat transfer from NC to PEA using the finite-element method and plotted the ΔT for PEA (averaged over the probe penetration depth). The range of κ (0.2-0.5 $W \cdot m^{-1} \cdot K^{-1}$) in these simulations is informed by thermal-transport studies on semiconductor NC films, which found similar κ values for a wide range of NC solids.[52] We find the ΔT for PEA is largely independent of the κ of the NC film (**Fig. 2f**), and the simulated temporal profiles of temperature rise match well with the measured kinetics of $\Delta R/R$. Inspection of the $\Delta R/R$ spectrum (**Fig. 2g**) shows that the maximal TCR at room temperature is centered at approximately 500 nm. A bi-exponential fit to the 500-nm $\Delta R/R$ kinetics distills exponential time constants of 1.2 μs and 9.2 μs in the 35-μs time window (**Fig. 2h**).

Spectrally tunable MIR detection with PET-supported PEA

With an understanding of the optical and thermal-transport properties of the ICO/PEA/PET stack, we designed and executed all-optical MIR photodetection experiments, as depicted in **Fig. 3a**. A bandpass filter of 500±5 nm defined a monochromatic probe at a wavelength where the sample exhibits the highest TCR. A broadband quasi-continuous-wave laser served as the MIR source, and five different MIR bandpass filters (Fig. S9) were used to define the wavelengths of MIR light incident on the sample. The MIR light was modulated by a mechanical chopper to enable lock-in detection of the variation in the reflected probe intensity. **Fig. 3b** summarizes the all-optical MIR detection results for PEA/PET coated with the three different ICO NCs measured at ambient temperature. Consistent with LSPR-enabled absorption (**Fig. 2c** and Fig. S10), the sensitivities of the samples all peak at the LSPR maxima wavelengths of the corresponding NC films. On top of this, all the samples show photo-responses at 3~3.5 μm, which arise from N-H stretching absorption of PEA. As summarized in Fig. S11, the measured lock-in voltage is linearly proportional to the incident MIR power, indicating a linear operational regime. Films on PET substrates show a sensitivity an order-of-magnitude higher than those on Si (**Fig. 3b**), which is in line with enhanced thermal retention with PET substrates (Fig. S4 vs. **Fig. 2d**). The mV-level lock-in voltage is a few thousandths of the PMT total output voltage (~0.5 V), from which we can estimate a relative change in reflectance to be less than one percent and hence a temperature modulation on the order of 1 K.

By varying the chopping frequency, we find the lock-in voltage increases with a decreasing chopping frequency over the explored range of 5000 Hz to 100 Hz (**Fig. 3c**). Such a monotonic relationship implies a long thermal time constant of at least 10 ms for the ICO/PEA/PET stacks. Thermal-transport simulations with impulsive heating at time zero (**Fig. 3d**) reveal that although the ΔT of PEA undergoes substantial decay by 100 μs (*i.e.*, in accordance with the IPVP results in **Fig. 2h**), the ΔT experiences a longer-lived tail. The thermal accumulation effect stemming from the long-lived component underpins the higher lock-in voltage achieved at lower chopping rates, and these results indicate that higher sensitivity can be achieved by further reducing the chopping rate at a cost of the detection bandwidth. To test the lowest MIR detection limit, we examined an ICO-1/PEA/PET sample under variable MIR powers at a wavelength of 3.33 μm with 100 Hz of MIR modulation frequency. As shown in **Fig. 3e**, the smallest detectable power density, which we define as when the signal is equivalent to the noise, reaches below 1 $nW \cdot \mu m^{-2}$. The ratio of the smallest detectable lock-in voltage (0.07 mV) and the PMT voltage (0.5 V) corresponds to a $\Delta R/R$ of ~0.014%.

Sensitivity enhancement by membrane-based structures

To further enhance the sensitivity to levels below the $nW \cdot \mu m^{-2}$ range, we then developed a unique membrane-based structure leveraging the anisotropic, wet chemical etching properties of silicon. The rationale behind this design is that a membrane-based architecture can suppress vertical heat flow channels and make in-plane heat flow less efficient. **Fig. 4a** shows a schematic of the obtained PEA/SiN_x/ICO structure. As illustrated in Fig. S12, the process begins with a commercially obtained low-stress SiN_x-coated Si wafer. For reasons described later, the thickness of SiN_x was chosen to be 265 nm throughout the work. Utilizing the well-established KOH wet-chemical etching method, we created tens-to-hundred μm-sized SiN_x membrane windows on Si substrates. A film of PEA was then spin-coated onto the SiN_x membrane, followed by the application of an ICO NC film, which was spin-coated onto the reverse side of the SiN_x membrane. We then evaluated the heat dissipation rates of the membrane structure through TR experiments. As shown in **Fig. 4b**, the decay of $\Delta R/R$ occurs over a duration exceeding one millisecond. This level of heat retention, much more effective than that of PET substrate-supported stacks (Figs. 2d and 2h), contributes to a significant improvement in MIR detectivity. As illustrated in **Fig. 4c**, we achieved an order of magnitude enhancement in detectivity, reaching the tens of $pW \cdot \mu m^{-2}$ range, all while maintaining a fixed MIR modulation frequency of 80 Hz.

To further enhance the sensitivity, we focus on the advantage of our all-optical detection scheme here, which permits the design of photonic structures to yield a larger magnitude of $\Delta R/R$ in response to a fixed, MIR light-induced temperature change in the PEA layer. Specifically, we exploited the nontrivial phase shift that occurs at the interface between the optically lossy PEA, especially near its exciton resonance, and a lossless dielectric material. As demonstrated in **Fig. 5a**, a thin dielectric coating onto the PEA enables enhanced absorption in PEA even with dielectric layers being considerably thinner than a quarter-wavelength ($\lambda/4$).[53] For illustrating this concept, we used the transfer-matrix approach to calculate the reflectance spectra of PEA covered by a

dielectric layer of varying thickness, using SiN_x as a model dielectric material. The calculated reflectance map in **Fig. 5b** shows that the interference effects caused by the phase shift at the PEA/SiN_x interface drastically alter the reflectance characteristics near the exciton resonance of PEA. The data further reveals that the changes in reflectance near the exciton resonance are periodic in the coating thickness and, crucially, for certain SiN_x coating thicknesses, specifically around 30, 150 and 270 nm, the reflectance can approach nearly zero, corresponding to complete optical absorption by the PEA.

Importantly, a low steady-state reflectance (R) is advantageous for our MIR detection scheme. This is because, by comparing the $\Delta R/R$ map in **Fig. 5c** and the reflectance in **Fig. 5b**, we find that a lower reflectance R leads to an increased relative change in reflectance ($\Delta R/R$, where steady-state reflectance R is the denominator). The $\Delta R/R$ is a critical factor in our signal readout for a fixed increase in exciton damping ($\Delta\gamma$) or, equivalently, a fixed temperature rise in the PEA layer. Theoretically, as the steady-state reflectance approaches zero, the value of $\Delta R/R$ tends to diverge. However, in practice, limitations to this divergence in enhancement exist, including those arising from the interfacial roughness between PEA and SiN_x, non-uniformity of the PEA film, and the thickness variation of the SiN_x, placing a ceiling on the maximum achievable MIR sensitivity. Despite these practical constraints, this dielectric-coating strategy still holds significant promise to further improve the sensitivity of our platform beyond the tens of $pW \cdot \mu m^{-2}$ range.

While the dielectric layer depicted in **Fig. 5a** can be deposited onto PEA using straightforward physical vapor deposition techniques, we found an intriguing alternative by treating the PEA-supporting SiN_x membrane itself as the dielectric layer. Notably, this approach is viable when the probe is incident on the SiN_x side rather than directly on the PEA. To accommodate this, we slightly modified our device structure used in **Fig. 4**. The new structure, ICO/PEA/SiN_x, and the associated configuration for MIR detection, is depicted in **Fig. 5d** (see Fig. S12 for sample fabrication details). We chose the SiN_x thickness to be 265 nm since it is close to the condition where $\Delta R/R$ reaches a high value (Fig. 5c). The measurements on ICO/PEA/SiN_x utilize a counter-propagating configuration, where the MIR light and visible probe light shine on the sample from opposing directions. Consistent with the transfer-matrix calculations, our measurements, as summarized in **Fig. 5e**, showed that when covered with the 265-nm thick SiN_x, the PEA displays a lower reflectance at its resonance dip and, importantly, a higher quality factor (*i.e.*, sharper reflectance dip), when compared to an uncovered PEA film, all measured at room temperature. The MIR sensitivity, manifested as the measured lock-in voltage in **Fig. 5e**, reaches a maximum when using a probe wavelength matching the reflectance dip. We tested the MIR sensitivity of the dielectric layer-enhanced device by using ICO-1 as the MIR absorber. MIR power-dependent measurements (**Fig. 5f**), utilizing a probe with 8 nm full-width-half-maximum (FWHM) in spectral bandwidth and a MIR pump centered at 3.33 μm, indicate that our structure achieves a remarkable sensitivity below 10 $pW \cdot \mu m^{-2}$, nearly two orders of magnitude more sensitive than a previous report utilizing ratiometric luminescence.[12]

To demonstrate the versatility of our approach, we expanded the detection from the MWIR range of 2~4.5 μm to the LWIR range at 10.6 μm, utilizing a CO_2 laser as the MIR excitation source. Here, we employed a simpler SiN_x/PEA bilayer structure, excluding the ICO NC layer. As shown in **Fig. 6a**, the infrared-active Si-N stretching mode of the SiN_x film leads to a broad and efficient vibrational absorption centered between 10 and 13 μm,[54] achieving ~50% absorption at 10.6 μm. A MIR sensitivity of 15.6 $pW \cdot \mu m^{-2}$ at this wavelength was achieved (**Fig. 6b**), which is comparable to the performance observed in the MWIR regime. Looking forward, we anticipate that the sensitivity of our scheme could be further improved by optimizing the SiN_x layer thickness (*i.e.*, better matching the conditions that produce maximum enhancement of $\Delta R/R$ in **Fig. 5c**), increasing the interfacial contact between SiN_x and PEA (potentially by adopting single-crystalline membranes), and simultaneously employing a probe light of a narrower spectral bandwidth with full-width-at-half-maximum of 1~2 nm. The last point is further illustrated in **Fig. 6c**, where stronger $\Delta R/R$ occurs at discrete, precise thicknesses of SiN_x when measured with a spectrally narrow probe. Cryogenic operation can also enable larger sensitivity due to a higher TCR of PEA at lower temperatures (**Fig. 1b** and Figs. S13-S14).

DISCUSSION

In summary, leveraging the ultralow κ and the large exciton-induced TCR (two properties rarely available together) of 2D-MHPs, we demonstrated a previously uncharted application of these materials in MIR thermal detection using $(PEA)_2PbI_4$ as a prototypical 2D-MHP. A comparison table (Table S1) shows that our proof-of-concept, 2D-MHP-based scheme compares favorably with other emerging methods for broadband MIR detection unburdened by materials' bandgaps. Stability test, as summarized in Fig. S16, shows that if the PEA film's back side is covered by a thin but compact dielectric layer, samples can be stable over several hours under a MIR power density two to three orders of magnitude larger than the detection limit. However, direct exposure of PEA's back side to ambient leads to sample degradation within a few tens of minutes under similar MIR power intensities. Looking beyond our current material of choice, other emerging hybrid layered materials might offer even lower thermal conductivity and higher TCR, leading to further advancements in MIR detectivity.[55,56] The concept demonstrated here can be extended toward realizing MIR imagers with lithographically defined 2D arrays of SiN_x membrane windows. Furthermore, our approach can be adapted for multiplexed MIR detection, capturing both intensity and wavelength information, by integrating pixelated plasmonic nano-antennas or by employing TCO NC pads with varying doping concentrations using ink-jet printing or other NC patterning techniques. The scope of light detection can be expanded into the far-infrared and terahertz range when 2D-MHPs are interfaced with optical resonators exhibiting strong plasmonic or phononic absorption at those spectral ranges.[57-60]

Materials and Methods

Sample Fabrication and Structural Characterization. *Materials:* Lead (II) iodide (99.999%) and γ-butyrolactone (≥99%) were obtained from Sigma-Aldrich; phenethylammonium iodide was obtained from Greatcell Solar. All chemicals were used as received. *Synthesis*: The perovskite thin films were fabricated by a two-step spin-coating method in ambient conditions. Specifically, the perovskite precursor solution was prepared by dissolving 0.9 mmol of lead (II) iodide and 1.8 mmol of phenethylammonium iodide into 0.54 mL of γ-butyrolactone. The substrates were treated with air plasma for 10 mins to ensure good solution wettability. The perovskite films were fabricated by dropping 50 μL of precursor solution onto the substrates and going through a two-step spin-coating program with 1000 rpm for 5 s and 3000 rpm for 45 s. Subsequently, the film was annealed at 80 °C on a hot plate for 15 mins. *Structural characterization:* The crystalline orientations of the perovskite films on various substrates were measured by X-ray diffraction (XRD) using θ-2θ scans with a Rigaku SmartLab X-ray diffractometer. The film thickness, morphology, and interfacial quality of multilayer stacks were examined by scanning electron microscopy (Hitachi SU8230).

Nanocrystal Synthesis. *Materials:* Cadmium acetylacetonate (99.9%), indium fluoride (99.9%), indium acetate (99.99%), octadecene (90%), and oleic acid (90%) were obtained from Sigma-Aldrich and used as received. Isopropanol and toluene for washing the particles were ACS grade from Fisher. *Synthesis*: Colloidal nanocrystals of doped cadmium oxide were prepared following literature procedures with small modifications.[51,61,62] All reactions consisted of 25 mL of octadecene, 1 mL oleic acid, and 1 mmol of total metal precursors; the precursors were loaded into a three-neck, 50 mL reaction flask and heated to 120 °C and held for 1 hour under vacuum (~1 torr), then heated rapidly under nitrogen atmosphere to the boiling point (~316 °C). The reaction was held at the boiling point of the solution for times between 5 and 40 minutes before the reaction medium turned from colorless to brown or green. After this color change, the reaction was maintained at 316 °C for an additional 10 minutes before being cooled back to room temperature by removal of a heating mantle. At room temperature, the reaction was decanted into two centrifuge tubes, 10 mL of toluene was added. Then isopropanol was added as an antisolvent until flocculation of the particles occurred. The samples were centrifuged for 5 minutes at 4000 rpm. Then, the pallet was re-dispersed in 5 mL of toluene. The solution was flocculated again with additional isopropanol and centrifuged for 5 minutes at 4000 rpm. The resulting pellet was re-dispersed in 3 mL of toluene and centrifuged at 2000 rpm for 2 minutes. The supernatant was saved. After one week, the solution was filtered through a 0.45-micrometer Teflon filter to remove precipitates. To change the frequency of the localized surface plasmon resonance, the type and amount of doping were controlled through the input metal precursors. Cadmium acetylacetonate was used as the cadmium precursor for 80% to 99% of the total metal content. Indium doping was achieved using between 1% and 20% indium acetate. Indium and fluorine co-doping was achieved by adding between 8% and 20% indium fluoride. The indium acetate doping concentrations in ICO-1 and ICO-2 were 20% and 5%, respectively. The indium fluoride doping concentration of

FICO was 15%. The micrographs of the nanocrystals were acquired by a JEOL 2100F transmission electron microscope operated at 200 kV with a 60,000X magnification.

Fabrication of Membrane Structure. *Silicon etching:* 19.2 mL of 45 wt.% KOH solution was added to 11.4 mL of H_2O to reach a 32 wt.% concentration. Then 3 mL of IPA was added to the 32 wt.% KOH solution to minimize the surface roughness of the etched samples. The solution was heated to 65 °C, and SiN_x/Si wafers (*i.e.*, 600 μm thick Si coated with 265 nm of low-stress SiN_x on both sides) were etched for 24 hours. Before dipping the SiN_x/Si wafer into the etch solution, a pinhole was created on its backside using a diamond scribe for enabling contact between Si and the KOH etcher. *Fabrication of the membrane samples:* $(PEA)_2PbI_4$ precursor solution was prepared by dissolving 0.75 mmol of lead (II) iodide and 1.5 mmol of PEAI into 0.5 mL of DMF. The etched SiN_x/Si wafers were treated with air plasma for 10 mins to ensure good solution wettability. $(PEA)_2PbI_4$ films were fabricated by spin-coating 50 μL of the as-prepared precursor solution onto preheated (150 °C) SiN_x/Si at 3000 rpm for 30 s with an acceleration of 1000 rpm/s. Then, 50 μL of ICO nanocrystal solution was spin-coated onto the substrates at 1000 rpm for 30 s with an acceleration of 500 rpm/s: (1) for the PEA/SiN_x/ICO membrane structure, the ICO nanocrystal solution was first spin-coated on the back side (*i.e.*, the etched side) of the SiN_x/Si substrate, then $(PEA)_2PbI_4$ solution was spin-coated on the front side; (2) for the ICO/PEA/SiN_x membrane structure, the ICO nanocrystal solution was spin-coated onto the $(PEA)_2PbI_4$ film, with the latter first deposited on the SiN_x/Si substrate. A schematic illustration for the fabrication of these two structures is shown in Fig. S12.

Finite-Element Simulations of Heat Transfer. The Heat Transfer module available in COMSOL Multiphysics 5.3a was used to simulate the transient thermal transport process along the cross-plane direction for comparison with experimental data. The calculation was performed in the time domain by solving the equation of heat conduction (*i.e.*, Fourier's law), $\rho C_P \frac{\partial T}{\partial t} + \nabla \cdot (-\kappa \nabla T) = 0$, where ρ is the mass density, C_P is the specific heat capacity, κ is the thermal conductivity, and T is the lattice temperature.

The heat capacity and thermal conductivity for silicon wafer were taken to be 710 $J \cdot kg^{-1} \cdot K^{-1}$ and 142.2 $W \cdot m^{-1} \cdot K^{-1}$, respectively. The thermal conductivity and heat capacity of polyethylene terephthalate (PET) were taken to be 0.19 $W \cdot m^{-1} \cdot K^{-1}$ and 1000 $J \cdot kg^{-1} \cdot K^{-1}$, respectively (Fire Safety Research Institute; https://materials.fsri.org/materialdetail/polyethylene-terephthalate-pet). The density, heat capacity, and thermal conductivity for cadmium oxide were taken from literature as 8101.4 $kg \cdot m^{-3}$, 43.1 $J \cdot mol^{-1} \cdot K^{-1}$ (or equivalently 335.6 $J \cdot kg^{-1} \cdot K^{-1}$), and 5.6~9.3 $W \cdot m^{-1} \cdot K^{-1}$, respectively.[63,64] The heat capacity of the TCO films was calculated by using a volume filling ratio of 41% for the inorganic core, 23% for the organic ligands, and 36% for the empty space between the particles. Such volume filling ratios were estimated by assuming that the inorganic core has a spherical shape with a diameter of 9.5 nm, the oleic ligands have a length of 1.5 nm, and the particles are randomly close-packed (*i.e.*, empty space between the particles occupies a volume fraction of 36%). The heat capacity[65] and mass density for oleic acid at 298 K were taken to be

1950 $J \cdot kg^{-1} \cdot K^{-1}$ and 895 $kg \cdot m^{-3}$, respectively. The heat capacity and mass density of the TCO film were determined to be 429.8 $J \cdot kg^{-1} \cdot K^{-1}$ and 3527.4 $kg \cdot m^{-3}$, respectively (by weighted sums of the inorganic and organic components comprising the film). The heat capacity for $(PEA)_2PbI_4$ was taken from the literature.[35]

When simulating the ICO/PEA/substrate stack, a uniform temperature rise of 10 K at time zero was assumed for the ICO film, whereas the initial temperature rise in $(PEA)_2PbI_4$ was taken to be zero, since the MIR absorption of ICO is about an order of magnitude higher than $(PEA)_2PbI_4$. When simulating the PEA/substrate stack (*i.e.*, no ICO), the initial temperature in $(PEA)_2PbI_4$ was peaked at the surface and decayed exponentially along the depth following the Beer-Lambert law. The absorption coefficient of the MIR pump in the $(PEA)_2PbI_4$ film was determined to be 6140 cm^{-1} using the data shown in Fig. 2c. In accordance with the penetration depth of the probe at ~500 nm (~140 nm; Fig. S1), the temperature of the top 140-nm thickness of the $(PEA)_2PbI_4$ film from the simulations was averaged, the normalized temporal decay of which was compared with the normalized, experimental $\Delta R/R$ at ~500 nm. It is to be noted that in the small temperature perturbation regime of the transient reflection experiments (as indicated by the fluence-independent decay kinetics; Fig. S15), the $\Delta R/R$ scales linearly with the lattice temperature, justifying the direct comparison between the simulated temperature decay and the measured kinetics of $\Delta R/R$.

Steady-State Optical Characterization. The steady-state optical reflectance experiments were performed using a customized micro-reflectance spectroscopy setup as reported previously,[38] with a slight modification that the light source was replaced by a supercontinuum laser (DISCO-2-UV, Leukos). A liquid-nitrogen cryostat (VPF-100, Lake Shore) was used to vary the sample's temperature from 78 to 300 K at a vacuum level better than 1×10^{-4} Torr. The MIR transmittance spectra were measured by Fourier-transform infrared spectroscopy (Nicolet 6700 FT-IR) with a mercury-cadmium-telluride detector.

Infrared-Pump Visible-Probe (IPVP) Transient Reflection (TR) Experiments. The IPVP TR measurements with a ns-to-ms time window were based on a setup reported previously.[44,66] Briefly, the idler output from a high-energy mid-infrared (MIR) optical parametric amplifier (OPA; Orpheus-ONE-HE, Light Conversion) served as the pump. The OPA was powered by a 170-fs Yb:KGW laser amplifier (Pharos, Light Conversion) with 0.9 mJ input energy operated at a 2 kHz repetition rate and reduced into 1 kHz by an optical chopper. The broadband probe pulses at a 2 kHz repetition rate were produced by a supercontinuum laser (DISCO-2-UV, Leukos), which was electronically triggered and delayed from the fs pump laser with a digital delay generator (DG645, Stanford Research Systems). The pump pulse was focused onto the sample using a CaF_2 lens of 200-mm focal length, which yielded a spot size of ~220 μm in diameter. The probe pulse was focused onto the sample using a 100-mm focal-length, achromatic doublet lens, providing a spot size of ~50 μm in diameter. The reflected probe pulses were captured and processed with a USB-coupled CMOS spectrometer (AvaSpec-ULS2048CL-EVO, Avantes).

All-Optical MIR Detection Measurements. MIR supercontinuum lasers (SC4500 from Thorlabs or Electro MIR 4.8 from Leukos) were used as the MIR light sources, which offer broadband output from 2.2 μm to 4.8 μm. The repetition rate of 50 MHz (for SC4500) or 250 kHz (for Electro MIR 4.8) is much higher than the chopping rate of less than 5 kHz. Compared to the thermal response time of the sample (*i.e.*, tens of μs; Fig. 1f) and the optical chopper frequency (100~5000 Hz), the high repetition-rate MIR lasers can be treated as continuous-wave sources. Several MIR bandpass filters (FB1900-200, FB3250-500, FB3330-150, FB3750-500, and FB4000-500, all from Thorlabs) were used to select the wavelength of the MIR light incident on the sample. The measured transmission spectra of the MIR filters are plotted in Fig. S9. An optical chopper was used to turn the MIR beam on and off at a frequency of 100 Hz for Fig. 3 (unless otherwise specified) or 80 Hz for Fig. 4 and Fig. 5. A CaF_2 lens was used to focus the MIR laser onto the sample with a spot size of 680 μm in diameter. For MIR measurement at 10.6 μm, we used a continuous-wave CO_2 gas laser, which was focused on the sample using a ZnSe lens. A combination of two ZnSe MIR linear polarizers was used to vary the power of the MIR laser incident on the sample.

For experiments shown in Fig. 3, the samples were probed by a high-power green light-emitting diode (LED) source (SOLIS-505C, Thorlabs). The output from the LED was wavelength-filtered by a 500-nm bandpass filter (10BPF10-500, Newport) or a 510-nm bandpass filter (FBH510-10, Thorlabs). For experiments shown in Fig. 4 and Fig. 5, the samples were probed by a supercontinuum laser coupled with a monochromator (Iceblink and Boreal, FYLA Inc.). The probe spectral width is approximately 8 nm in its full width at half maximum. The probe light reflected by the sample was directed into a photomultiplier tube (H10722-20, Hamamatsu), whose voltage output was measured by a lock-in amplifier (SR860, Stanford Research Systems) with the optical chopper providing the reference signal. The control voltage of the PMT was adjusted to yield a constant output voltage of 0.5 volts in the measurements for Fig. 3, or 0.1 volts in the measurements for Fig. 4 and Fig. 5, to enable comparison between different samples.

Supplementary Materials

Materials and Methods

Figs. S1 to S15, Table S1

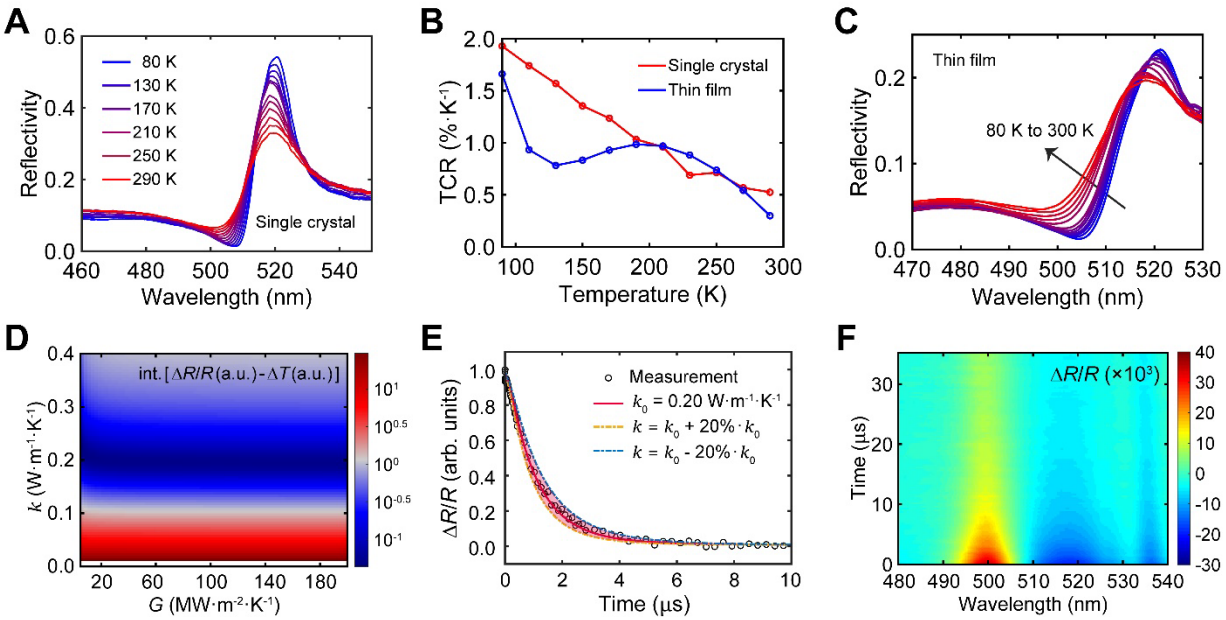

Fig. 1. TCR and thermal transport properties of PEA. (**A**) Temperature-dependent reflectance spectra of PEA single crystal. (**B**) Temperature-dependent TCR at the reflectance-dip wavelength for PEA single crystal and spin-coated film. (**C**) Temperature-dependent reflectance spectra of a spin-coated PEA film with ~1 μm thickness. (**D**) Time-integrated difference between normalized $\Delta R/R$ at the reflectance-dip wavelength from IPVP experiments and normalized ΔT from finite-element simulations, shown as a function of κ and G. Note that the color bar is shown in $\log_{10}$ scale (*i.e.*, blue color indicates low fitting error). (**E**) Decay kinetics of $\Delta R/R$ at the reflectance-dip wavelength and the fitted decay of ΔT with finite-element simulations. The shaded area represents an 80% confidence band. The experimental data is taken from Fig. S4. (**F**) Transient spectral map of $\Delta R/R$ for a 940 nm-thick PEA film on PET measured at room temperature (pump wavelength: 3170 nm; fluence: 3.6 mJ·cm^{-2}).

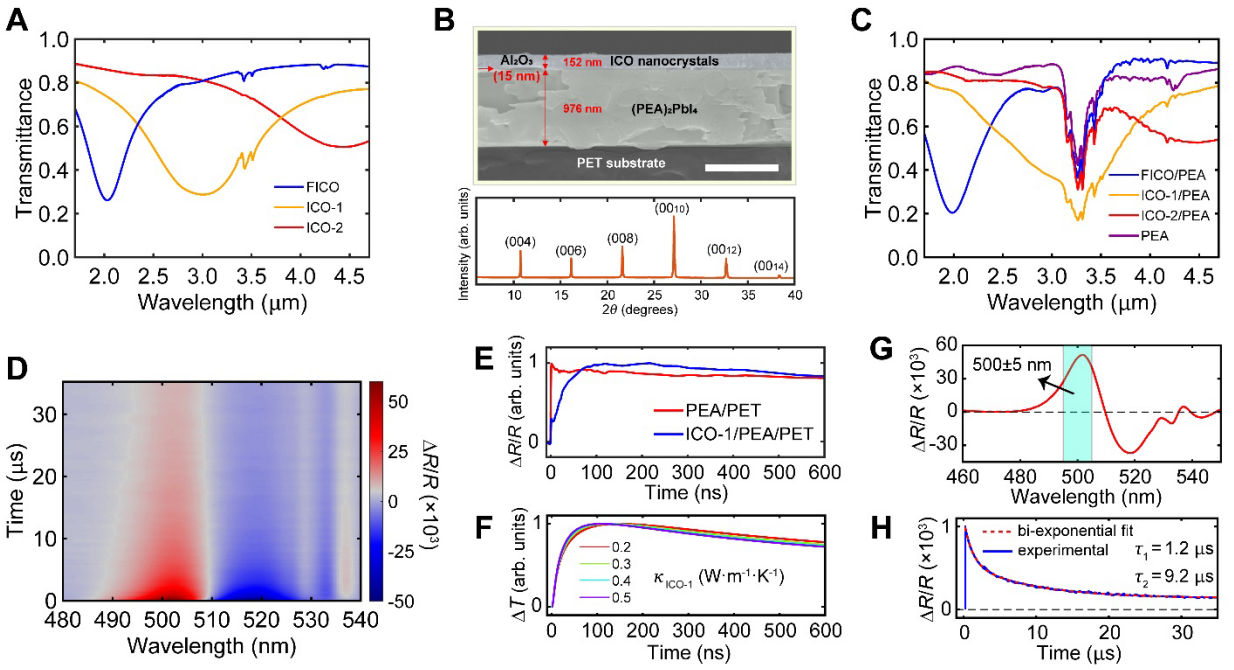

Fig. 2. Optical and structural characterization of PEA films coated with ICO NCs. (**A**) MIR transmittance spectra of ICO NC films with different doping concentrations on sapphire substrates. (**B**) Cross-sectional SEM image of ICO-1/PEA/PET (scalebar: 1 μm) and its XRD pattern (the out-of-plane XRD peaks of PEA are indexed). (**C**) MIR transmission spectra of CaF_2 substrate-supported PEA films with and without ICO NC films on top. (**D**) Transient $\Delta R/R$ spectral map of ICO-1/PEA/PET at room temperature (pump wavelength: 3170 nm; fluence: 3.9 mJ·cm^{-2}). (**E**) Comparison of $\Delta R/R$ kinetics at 500 nm between PEA/PET and ICO-1/PEA/PET. (**F**) Simulated decays of ΔT for PEA (averaged for the top 140 nm, which is the probe penetration depth) in ICO-1/PEA/PET, obtained with various values of κ for the ICO-1. (**G**) Transient $\Delta R/R$ spectrum at 100 ns, and (**H**) $\Delta R/R$ kinetics at 500 nm and its bi-exponential fit; data is taken from (**D**).

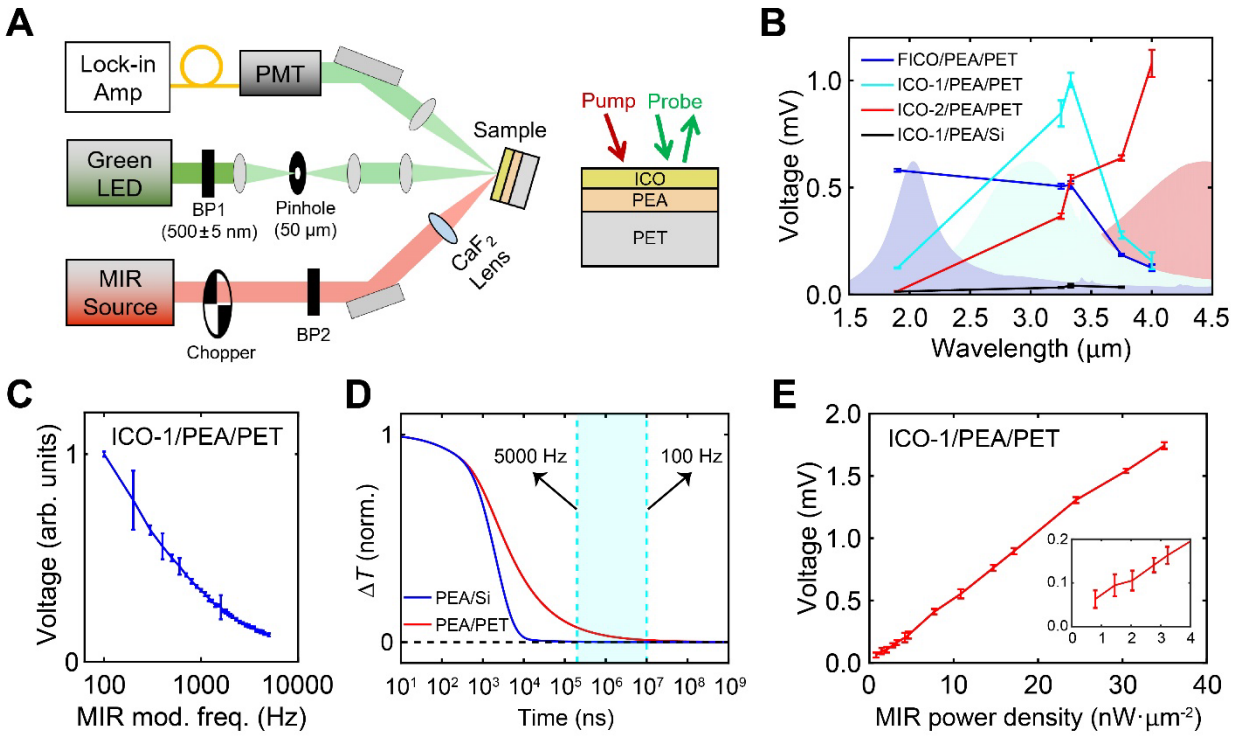

Fig. 3. Spectrally tunable, all-optical MIR photodetection using ICO/PEA/PET stacks. (**A**) Schematic depiction of the all-optical MIR photodetection setup; BP1 (BP2) is the bandpass filter for the visible probe (the MIR pump). (**B**) Lock-in voltage for PEA/PET coated with the three different ICO-NC films; data for PEA/Si coated with ICO-1 measured at the same MIR power density is also shown for comparison. Shaded regions correspond to ICO NC absorbance in arbitrary units. (**C**) Lock-in voltage of ICO-1/PEA/PET as a function of the chopper frequency. (**D**) Finite-element simulated decays of the temperature averaged over the probe penetration depth (140 nm) of a 940-nm thick PEA film deposited on Si and PET substrates. (**E**) Lock-in voltage of ICO-1/PEA/PET versus MIR (3.33 μm) power density (inset shows the range from 0 to 4 $nW \cdot \mu m^{-2}$).

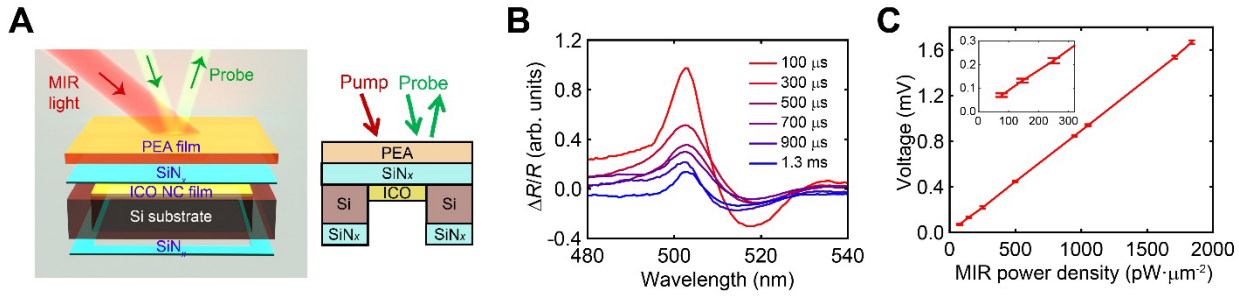

Fig. 4. Thin membrane-based structure exhibits <100 pW·μm^{-2} sensitivity. (**A**) Schematic illustration of the PEA/SiN$_x$/ICO-1 membrane structure supported by a Si substrate (Left: 3D illustration; Right: 2D view). (**B**) Transient $\Delta R/R$ spectra of a floating PEA membrane for varying delay times (100 μs to 1.3 ms). (**C**) Lock-in voltage of PEA/SiN$_x$/ICO-1 on Si versus MIR (3.33 μm) power density (inset shows the range from 0 to 300 pW·μm^{-2}).

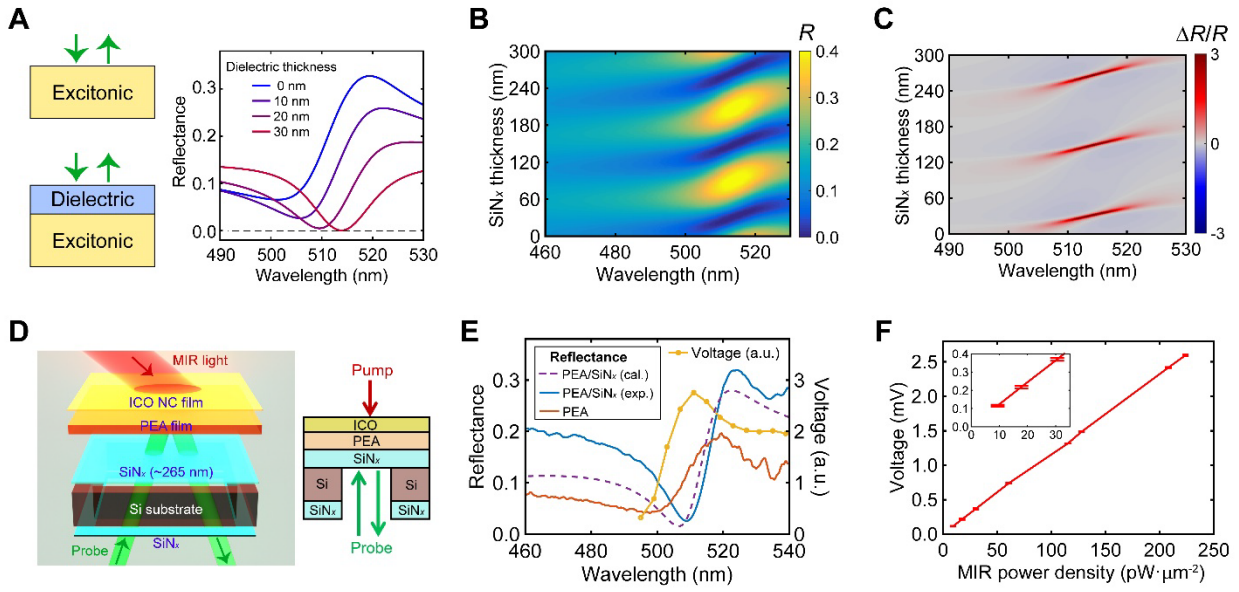

Fig. 5. Thin membrane-based structure incorporating a dielectric coating enables <10 pW·μm^{-2} sensitivity. (**A**) Demonstration of the dielectric coating-induced decrease in reflectance near the excitonic resonance of PEA. (**B**) Transfer matrix-calculated reflectance spectra of PEA film covered by SiN_x (refractive index $n = 2.19$) with SiN_x thickness varied from 0 to 300 nm. (**C**) Color-coded map of $\Delta R/R = \left(R_{\gamma=77\ \mathrm{meV}} - R_{\gamma=67\ \mathrm{meV}}\right)/R_{\gamma=67\ \mathrm{meV}}$ plotted as a function of wavelength and SiN_x thickness. Here, $\gamma = 67$ meV is the fitted Lorentzian damping factor for PEA at ambient temperature (Fig. S1) and, without the loss of generality, the increase of γ from 67 to 77 meV is assumed to be induced by MIR light irradiation. (**D**) Schematic drawing of the inverted ICO/PEA/SiN_x structure on Si substrate and the associated measurement scheme (Left: 3D illustration; Right: 2D view). (**E**) Reflectance spectra for PEA covered with a 265-nm thick SiN_x (calculated: purple-dashed; measured: blue) and for PEA without any SiN_x coverage (red, taken from data in Fig. 1c). The measured lock-in voltage as a function of probe wavelength is shown in yellow for a PEA covered with a 265-nm thick SiN_x. (**F**) Lock-in voltage of ICO-1/PEA/SiN_x versus MIR (3.33 μm in wavelength) power density (inset shows the range from 0 to 35 pW·μm^{-2}).

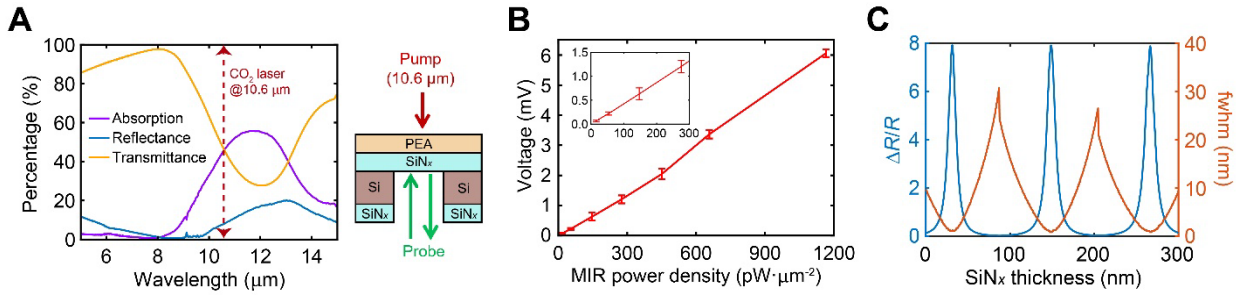

Fig. 6. Long-wave infrared (LWIR) detection at 10.6 μm wavelength. (**A**) Left: experimental transmittance, experimental reflectance, and calculated absorption for a 265-nm thick SiN_x membrane from 5 to 15 μm. Right: schematic drawing of the sample and measurement configuration. (**B**) Lock-in voltage of PEA/SiN_x versus MIR (10.6 μm in wavelength) power density (inset shows the range from 0 to 300 pW·μm^{-2}). (**C**) The maximum value of $\Delta R/R$ as a function of the thickness of the SiN_x layer on top of PEA, and the associated full-width-half-maximum of the peak of $\Delta R/R$, both calculated from the transfer-matrix calculated data in panel (**C**).

Acknowledgements

Funding: This work was primarily supported by the Office of Naval Research under Grant N00014-24-1-2045 (Y.L. and P.G.). Work performed at the Center for Nanoscale Materials, a U.S. Department of Energy Office of Science User Facility, was supported by the U.S. DOE, Office of Basic Energy Sciences, under Contract No. DE-AC02-06CH11357 (B.T.D.). The work was partially supported by the National Science Foundation under Grant DMR-2313648 (S.L. and D.C.).

Author contributions: P.G. conceived and supervised the project. Y.L., B.T.D., S.L. and D.C. fabricated the samples. Y.L. and P.G. performed the measurements with help from S.L., D. C. and C.A.K. D.C. performed thermal transport simulations. A.Y. helped with SiN_x membrane fabrication. P.G. wrote the manuscript with inputs from Y.L. All authors edited and commented on the manuscript.

*Corresponding author (email: peijun.guo@yale.edu)

Competing interests: P.G. an inventor on a pending patent filed by Yale University (YV 8733). The authors declare no other competing interests.

Data and materials availability: All data needed to evaluate the conclusions in the study are present in the main text and/or the Supplementary Materials.

REFERENCES AND NOTES

1. A. V. Muraviev, V. O. Smolski, Z. E. Loparo, and K. L. Vodopyanov, Massively parallel sensing of trace molecules and their isotopologues with broadband subharmonic mid-infrared frequency combs. *Nat. Photonics* **12***,* 209-214 (2018).

2. H. Lin, L. Li, Y. Zou, S. Danto, J. D. Musgraves, K. Richardson, S. Kozacik, M. Murakowski, D. Prather, P. T. Lin, V. Singh, A. Agarwal, L. C. Kimerling, and J. Hu, Demonstration of high-Q mid-infrared chalcogenide glass-on-silicon resonators. *Opt. Lett.* **38***,* 1470-1472 (2013).

3. C. R. Petersen, N. Prtljaga, M. Farries, J. Ward, B. Napier, G. R. Lloyd, J. Nallala, N. Stone, and O. Bang, Mid-infrared multispectral tissue imaging using a chalcogenide fiber supercontinuum source. *Opt. Lett.* **43***,* 999-1002 (2018).

4. S. P. Garaba, J. Aitken, B. Slat, H. M. Dierssen, L. Lebreton, O. Zielinski, and J. Reisser, Sensing ocean plastics with an airborne hyperspectral shortwave infrared imager. *Environ. Sci. Technol.* **52***,* 11699-11707 (2018).

5. K. Zou, K. Pang, H. Song, J. Fan, Z. Zhao, H. Song, R. Zhang, H. Zhou, A. Minoofar, C. Liu, X. Su, N. Hu, A. McClung, M. Torfeh, A. Arbabi, M. Tur, and A. E. Willner, High-capacity free-space optical communications using wavelength- and mode-division-multiplexing in the mid-infrared region. *Nat. Commun.* **13***,* 7662 (2022).

6. S. McSherry, M. Webb, J. Kaufman, Z. Deng, A. Davoodabadi, T. Ma, E. Kioupakis, K. Esfarjani, J. T. Heron, and A. Lenert, Nanophotonic control of thermal emission under extreme temperatures in air. *Nat. Nanotechnol.* **17***,* 1104-1110 (2022).

7. R. K. Bhan and V. Dhar, Recent infrared detector technologies, applications, trends and development of HgCdTe based cooled infrared focal plane arrays and their characterization. *Opto-Electron. Rev.* **27***,* 174-193 (2019).

8. A. Rogalski, HgCdTe infrared detector material: history, status and outlook. *Rep. Prog. Phys.* **68***,* 2267-2336 (2005).

9. P. V. K. Yadav, I. Yadav, B. Ajitha, A. Rajasekar, S. Gupta, and Y. Ashok Kumar Reddy, Advancements of uncooled infrared microbolometer materials: a review. *Sens. Actuators, A* **342***,* 113611 (2022).

10. H. Wang, X. Yi, G. Huang, J. Xiao, X. Li, and S. Chen, IR microbolometer with self-supporting structure operating at room temperature. *Infrared Phys. Technol.* **45***,* 53-57 (2004).

11. A. Xomalis, X. Zheng, R. Chikkaraddy, Z. Koczor-Benda, E. Miele, E. Rosta, G. A. E. Vandenbosch, A. Martínez, and J. J. Baumberg, Detecting mid-infrared light by molecular frequency upconversion in dual-wavelength nanoantennas. *Science* **374***,* 1268-1271 (2021).

12. L. Liang, C. Wang, J. Chen, Q. J. Wang, and X. Liu, Incoherent broadband mid-infrared detection with lanthanide nanotransducers. *Nat. Photonics* **16***,* 712-717 (2022).

13. D. Wu, Y. Ma, Y. Niu, Q. Liu, T. Dong, S. Zhang, J. Niu, H. Zhou, J. Wei, Y. Wang, Z. Zhao, and N. Wang, Ultrabroadband photosensitivity from visible to terahertz at room temperature. *Sci. Adv.* **4**, eaao3057 (2018).

14. S. Castilla, I. Vangelidis, V.-V. Pusapati, J. Goldstein, M. Autore, T. Slipchenko, K. Rajendran, S. Kim, K. Watanabe, T. Taniguchi, L. Martín-Moreno, D. Englund, K.-J. Tielrooij, R. Hillenbrand, E. Lidorikis, and F. H. L. Koppens, Plasmonic antenna coupling to hyperbolic phonon-polaritons for sensitive and fast mid-infrared photodetection with graphene. *Nat. Commun.* **11**, 4872 (2020).

15. L. Zeng, D. Wu, J. Jie, X. Ren, X. Hu, S. P. Lau, Y. Chai, and Y. H. Tsang, Van der Waals epitaxial growth of Mosaic-like 2D platinum ditelluride layers for room-temperature mid-infrared photodetection up to 10.6 μm. *Adv. Mater.* **32**, 2004412 (2020).

16. A. Kojima, K. Teshima, Y. Shirai, and T. Miyasaka, Organometal halide perovskites as visible-light sensitizers for photovoltaic cells. *J. Am. Chem. Soc.* **131***,* 6050-6051 (2009).

17. S. Bai, P. Da, C. Li, Z. Wang, Z. Yuan, F. Fu, M. Kawecki, X. Liu, N. Sakai, J. T.-W. Wang, S. Huettner, S. Buecheler, M. Fahlman, F. Gao, and H. J. Snaith, Planar perovskite solar cells with long-term stability using ionic liquid additives. *Nature* **571***,* 245-250 (2019).

18. H. Wei, Y. Fang, P. Mulligan, W. Chuirazzi, H.-H. Fang, C. Wang, B. R. Ecker, Y. Gao, M. A. Loi, L. Cao, and J. Huang, Sensitive X-ray detectors made of methylammonium lead tribromide perovskite single crystals. *Nat. Photonics* **10***,* 333-339 (2016).

19. B. R. Sutherland and E. H. Sargent, Perovskite photonic sources. *Nat. Photonics* **10***,* 295-302 (2016).

20. S. Tan, T. Huang, I. Yavuz, R. Wang, T. W. Yoon, M. Xu, Q. Xing, K. Park, D.-K. Lee, C.-H. Chen, R. Zheng, T. Yoon, Y. Zhao, H.-C. Wang, D. Meng, J. Xue, Y. J. Song, X. Pan, N.-G. Park, J.-W. Lee, and Y. Yang, Stability-limiting heterointerfaces of perovskite photovoltaics. *Nature* **605***,* 268-273 (2022).

21. Z. Xiao, R. A. Kerner, L. Zhao, N. L. Tran, K. M. Lee, T.-W. Koh, G. D. Scholes, and B. P. Rand, Efficient perovskite light-emitting diodes featuring nanometre-sized crystallites. *Nat. Photonics* **11***,* 108-115 (2017).

22. J.-P. Correa-Baena, Y. Luo, T. M. Brenner, J. Snaider, S. Sun, X. Li, M. A. Jensen, N. T. P. Hartono, L. Nienhaus, S. Wieghold, J. R. Poindexter, S. Wang, Y. S. Meng, T. Wang, B. Lai, M. V. Holt, Z. Cai, M. G. Bawendi, L. Huang, T. Buonassisi, and D. P. Fenning, Homogenized halides and alkali cation segregation in alloyed organic-inorganic perovskites. *Science* **363***,* 627-631 (2019).

23. A. D. Wright, C. Verdi, R. L. Milot, G. E. Eperon, M. A. Pérez-Osorio, H. J. Snaith, F. Giustino, M. B. Johnston, and L. M. Herz, Electron–phonon coupling in hybrid lead halide perovskites. *Nat. Commun.* **7***,* 11755 (2016).

24. Y. Guo, O. Yaffe, T. D. Hull, J. S. Owen, D. R. Reichman, and L. E. Brus, Dynamic emission Stokes shift and liquid-like dielectric solvation of band edge carriers in lead-halide perovskites. *Nat. Commun.* **10***,* 1175 (2019).

25. X. Gong, O. Voznyy, A. Jain, W. Liu, R. Sabatini, Z. Piontkowski, G. Walters, G. Bappi, S. Nokhrin, O. Bushuyev, M. Yuan, R. Comin, D. McCamant, S. O. Kelley, and E. H. Sargent, Electron–phonon interaction in efficient perovskite blue emitters. *Nat. Mater.* **17***,* 550-556 (2018).

26. K. Miyata, D. Meggiolaro, M. T. Trinh, P. P. Joshi, E. Mosconi, S. C. Jones, F. De Angelis, and X.-Y. Zhu, Large polarons in lead halide perovskites. *Sci. Adv.* **3***,* e1701217 (2017).

27. B. Guzelturk, T. Winkler, T. W. J. Van de Goor, M. D. Smith, S. A. Bourelle, S. Feldmann, M. Trigo, S. W. Teitelbaum, H.-G. Steinrück, G. A. de la Pena, R. Alonso-Mori, D. Zhu, T. Sato, H. I. Karunadasa, M. F. Toney, F. Deschler, and A. M. Lindenberg, Visualization of dynamic polaronic strain fields in hybrid lead halide perovskites. *Nat. Mater.* **20***,* 618-623 (2021).

28. B. Saparov and D. B. Mitzi, Organic–inorganic perovskites: structural versatility for functional materials design. *Chem. Rev.* **116***,* 4558-4596 (2016).

29. X. Li, J. M. Hoffman, and M. G. Kanatzidis, The 2D halide perovskite rulebook: how the spacer influences everything from the structure to optoelectronic device efficiency. *Chem. Rev.* **121***,* 2230-2091 (2021).

30. H. Tsai, W. Nie, J.-C. Blancon, C. C. Stoumpos, R. Asadpour, B. Harutyunyan, A. J. Neukirch, R. Verduzco, J. J. Crochet, S. Tretiak, L. Pedesseau, J. Even, M. A. Alam, G. Gupta, J. Lou, P. M. Ajayan, M. J. Bedzyk, M. G. Kanatzidis, and A. D. Mohite, High-efficiency two-dimensional Ruddlesden–Popper perovskite solar cells. *Nature* **536***,* 312-316 (2016).

31. C. Katan, N. Mercier, and J. Even, Quantum and dielectric confinement effects in lower-dimensional hybrid perovskite semiconductors. *Chem. Rev.* **119***,* 3140-3192 (2019).

32. D. B. Straus and C. R. Kagan, Electrons, excitons, and phonons in two-dimensional hybrid perovskites: connecting structural, optical, and electronic properties. *J. Phys. Chem. Lett.* **9***,* 1434-1447 (2018).

33. J.-C. Blancon, J. Even, C. C. Stoumpos, M. G. Kanatzidis, and A. D. Mohite, Semiconductor physics of organic–inorganic 2D halide perovskites. *Nat. Nanotechnol.* **15***,* 969-985 (2020).

34. P. Guo, C. C. Stoumpos, L. Mao, S. Sadasivam, J. B. Ketterson, P. Darancet, M. G. Kanatzidis, and R. D. Schaller, Cross-plane coherent acoustic phonons in two-dimensional organic-inorganic hybrid perovskites. *Nat. Commun.* **9***,* 2019 (2018).

35. A. Giri, A. Z. Chen, A. Mattoni, K. Aryana, D. Zhang, X. Hu, S.-H. Lee, J. J. Choi, and P. E. Hopkins, Ultralow thermal conductivity of two-dimensional metal halide perovskites. *Nano Lett.* **20***,* 3331-3337 (2020).

36. C. Li, H. Ma, T. Li, J. Dai, M. A. J. Rasel, A. Mattoni, A. Alatas, M. G. Thomas, Z. W. Rouse, A. Shragai, S. P. Baker, B. J. Ramshaw, J. P. Feser, D. B. Mitzi, and Z. Tian, Remarkably weak anisotropy in thermal conductivity of two-dimensional hybrid perovskite butylammonium lead iodide crystals. *Nano Lett.* **21***,* 3708-3714 (2021).

37. Y. Liu, Y. Zhang, Z. Yang, H. Ye, J. Feng, Z. Xu, X. Zhang, R. Munir, J. Liu, P. Zuo, Q. Li, M. Hu, L. Meng, K. Wang, D.-M. Smilgies, G. Zhao, H. Xu, Z. Yang, A. Amassian, J. Li, K. Zhao, and S. Liu, Multi-inch single-crystalline perovskite membrane for high-detectivity flexible photosensors. *Nat. Commun.* **9***,* 5302 (2018).

38. S. Li, X. Li, C. A. Kocoj, X. Ji, S. Yuan, E. C. Macropulos, C. C. Stoumpos, F. Xia, L. Mao, M. G. Kanatzidis, and P. Guo, Ultrafast excitonic response in two-dimensional hybrid perovskites driven by intense midinfrared pulses. *Phys. Rev. Lett.* **129***,* 177401 (2022).

39. Y. Li, A. Chernikov, X. Zhang, A. Rigosi, H. M. Hill, A. M. van der Zande, D. A. Chenet, E.-M. Shih, J. Hone, and T. F. Heinz, Measurement of the optical dielectric function of monolayer transition-metal dichalcogenides: MoS_2, $MoSe_2$, WS_2, and WSe_2. *Phys. Rev. B* **90***,* 205422 (2014).

40. G. Scuri, Y. Zhou, A. A. High, D. S. Wild, C. Shu, K. De Greve, L. A. Jauregui, T. Taniguchi, K. Watanabe, P. Kim, M. D. Lukin, and H. Park, Large excitonic reflectivity of monolayer $MoSe_2$ encapsulated in hexagonal boron nitride. *Phys. Rev. Lett.* **120***,* 037402 (2018).

41. P. Guo, W. Huang, C. C. Stoumpos, L. Mao, J. Gong, L. Zeng, B. T. Diroll, Y. Xia, X. Ma, D. J. Gosztola, T. Xu, J. B. Ketterson, M. J. Bedzyk, A. Facchetti, T. J. Marks, M. G. Kanatzidis, and R. D. Schaller, Hyperbolic dispersion arising from anisotropic excitons in two-dimensional perovskites. *Phys. Rev. Lett.* **121***,* 127401 (2018).

42. O. Yaffe, A. Chernikov, Z. M. Norman, Y. Zhong, A. Velauthapillai, A. van der Zande, J. S. Owen, and T. F. Heinz, Excitons in ultrathin organic-inorganic perovskite crystals. *Phys. Rev.B* **92***,* 045414 (2015).

43. B. Li, J. Xu, C. A. Kocoj, S. Li, Y. Li, D. Chen, S. Zhang, L. Dou, and P. Guo, Dual-hyperspectral optical pump–probe microscopy with single-nanosecond time resolution. *J. Am. Chem. Soc.* **146***,* 2187-2195 (2024).

44. S. Li, Z. Dai, L. Li, N. P. Padture, and P. Guo, Time-resolved vibrational-pump visible-probe spectroscopy for thermal conductivity measurement of metal-halide perovskites. *Rev. Sci. Instrum.* **93***,* 053003 (2022).

45. P. Jiang, X. Qian, and R. Yang, Tutorial: Time-domain thermoreflectance (TDTR) for thermal property characterization of bulk and thin film materials. *J. Appl. Phys.* **124***,* 161103 (2018).

46. H. Kizuka, T. Yagi, J. Jia, Y. Yamashita, S. Nakamura, N. Taketoshi, and Y. Shigesato, Temperature dependence of thermal conductivity of VO_2 thin films across metal–insulator transition. *Jpn. J. Appl. Phys.* **54***,* 053201 (2015).

47. D.-W. Oh, C. Ko, S. Ramanathan, and D. G. Cahill, Thermal conductivity and dynamic heat capacity across the metal-insulator transition in thin film VO_2. *Appl. Phys. Lett.* **96***,* 151906 (2010).

48. A. Boltasseva and H. A. Atwater, Low-loss plasmonic metamaterials. *Science* **331***,* 290-291 (2011).

49. P. Guo, R. D. Schaller, J. B. Ketterson, and R. P. H. Chang, Ultrafast switching of tunable infrared plasmons in indium tin oxide nanorod arrays with large absolute amplitude. *Nat. Photonics* **10***,* 267-273 (2016).

50. A. Agrawal, S. H. Cho, O. Zandi, S. Ghosh, R. W. Johns, and D. J. Milliron, Localized surface plasmon resonance in semiconductor nanocrystals. *Chem. Rev.* **118***,* 3121-3207 (2018).

51. T. R. Gordon, T. Paik, D. R. Klein, G. V. Naik, H. Caglayan, A. Boltasseva, and C. B. Murray, Shape-dependent plasmonic response and directed self-assembly in a new semiconductor building block, indium-doped cadmium oxide (ICO). *Nano Lett.* **13***,* 2857-2863 (2013).

52. W.-L. Ong, S. M. Rupich, D. V. Talapin, A. J. H. McGaughey, and J. A. Malen, Surface chemistry mediates thermal transport in three-dimensional nanocrystal arrays. *Nat. Mater.* **12***,* 410-415 (2013).

53. M. A. Kats, R. Blanchard, P. Genevet, and F. Capasso, Nanometre optical coatings based on strong interference effects in highly absorbing media. *Nat. Mater.* **12***,* 20-24 (2013).

54. F. Liu, S. Ward, L. Gedvilas, B. Keyes, B. To, Q. Wang, E. Sanchez, and S. Wang, Amorphous silicon nitride deposited by hot-wire chemical vapor deposition. *J. Appl. Phys.* **96***,* 2973-2979 (2004).

55. W. Paritmongkol, T. Sakurada, W. S. Lee, R. Wan, P. Müller, and W. A. Tisdale, Size and quality enhancement of 2D semiconducting metal–organic chalcogenolates by amine addition. *J. Am. Chem. Soc.* **143***,* 20256-20263 (2021).

56. W. Li, Z. Wang, F. Deschler, S. Gao, R. H. Friend, and A. K. Cheetham, Chemically diverse and multifunctional hybrid organic–inorganic perovskites. *Nat. Rev. Mater.* **2***,* 16099 (2017).

57. M. Liu, H. Y. Hwang, H. Tao, A. C. Strikwerda, K. Fan, G. R. Keiser, A. J. Sternbach, K. G. West, S. Kittiwatanakul, J. Lu, S. A. Wolf, F. G. Omenetto, X. Zhang, K. A. Nelson, and R. D. Averitt, Terahertz-field-induced insulator-to-metal transition in vanadium dioxide metamaterial. *Nature* **487***,* 345-348 (2012).

58. J. D. Caldwell, I. Vurgaftman, J. G. Tischler, O. J. Glembocki, J. C. Owrutsky, and T. L. Reinecke, Atomic-scale photonic hybrids for mid-infrared and terahertz nanophotonics. *Nat. Nanotechnol.* **11***,* 9-15 (2016).

59. S. Dai, Q. Ma, M. K. Liu, T. Andersen, Z. Fei, M. D. Goldflam, M. Wagner, K. Watanabe, T. Taniguchi, M. Thiemens, F. Keilmann, G. C. A. M. Janssen, S. E. Zhu, P. Jarillo-Herrero, M. M. Fogler, and D. N. Basov, Graphene on hexagonal boron nitride as a tunable hyperbolic metamaterial. *Nat Nanotechnol* **10***,* 682-686 (2015).

60. C. Wang, S. Huang, Q. Xing, Y. Xie, C. Song, F. Wang, and H. Yan, Van der Waals thin films of WTe_2 for natural hyperbolic plasmonic surfaces. *Nat. Commun.* **11***,* 1158 (2020).

61. X. Ye, J. Fei, B. T. Diroll, T. Paik, and C. B. Murray, Expanding the spectral tunability of plasmonic resonances in doped metal-oxide nanocrystals through cooperative cation–anion codoping. *J. Am. Chem. Soc.* **136**, 11680-11686 (2014).

62. B. T. Diroll, T. R. Gordon, E. A. Gaulding, D. R. Klein, T. Paik, H. J. Yun, E. D. Goodwin, D. Damodhar, C. R. Kagan, and C. B. Murray, Synthesis of n-type plasmonic oxide nanocrystals and the optical and electrical characterization of their transparent conducting films. *Chem. Mater.* **26**, 4579-4588 (2014).

63. R. W. Millar, The heat capacity at low temperatures of zinc oxide and of cadmium oxide. *J. Am. Chem. Soc.* **50**, 2653-2656 (1928).

64. L. Lindsay and D. S. Parker, Calculated transport properties of CdO: thermal conductivity and thermoelectric power factor. *Phys. Rev. B* **92**, 144301 (2015).

65. F. O. Cedeño, M. M. Prieto, and J. Xiberta, Measurements and estimate of heat capacity for some pure fatty acids and their binary and ternary mixtures. *J. Chem. Eng. Data* **45**, 64-69 (2000).

66. S. Li, Z. Dai, C. A. Kocoj, E. I. Altman, N. P. Padture, and P. Guo, Photothermally induced, reversible phase transition in methylammonium lead triiodide. *Matter* **6**, 460-74 (2023).

67. A. Xomalis, X. Zheng, R. Chikkaraddy, Z. Koczor-Benda, E. Miele, E. Rosta, G. A. E. Vandenbosch, A. Martínez, and J. J. Baumberg, Detecting mid-infrared light by molecular frequency upconversion in dual-wavelength nanoantennas. *Science* **374**, 1268-1271 (2021).

68. D. Wu, Y. Ma, Y. Niu, Q. Liu, T. Dong, S. Zhang, J. Niu, H. Zhou, J. Wei, Y. Wang, Z. Zhao, and N. Wang, Ultrabroadband photosensitivity from visible to terahertz at room temperature. *Sci. Adv.* **4**, eaao3057 (2018).

69. D. K. Efetov, R.-J. Shiue, Y. Gao, B. Skinner, E. D. Walsh, H. Choi, J. Zheng, C. Tan, G. Grosso, C. Peng, J. Hone, K. C. Fong, and D. Englund, Fast thermal relaxation in cavity-coupled graphene bolometers with a Johnson noise read-out. *Nat. Nanotechnol.* **13**, 797-801 (2018).

70. J. Shi, D. Yoo, F. Vidal-Codina, C.-W. Baik, K.-S. Cho, N.-C. Nguyen, H. Utzat, J. Han, A. M. Lindenberg, V. Bulović, M. G. Bawendi, J. Peraire, S.-H. Oh, and K. A. Nelson, A room-temperature polarization-sensitive CMOS terahertz camera based on quantum-dot-enhanced terahertz-to-visible photon upconversion. *Nat. Nanotechnol.* **17**, 1288-1293 (2022).

71. C. Chen, C. Li, S. Min, Q. Guo, Z. Xia, D. Liu, Z. Ma, and F. Xia, Ultrafast silicon nanomembrane microbolometer for long-wavelength infrared light detection. *Nano Lett.* **21**, 8385-8392 (2021).

Supplementary Materials for

Mid-infrared photodetection with 2D metal halide perovskites at ambient temperature

Yanyan Li *et al.*

This PDF file includes:

Fig. S1 to S16

Table S1

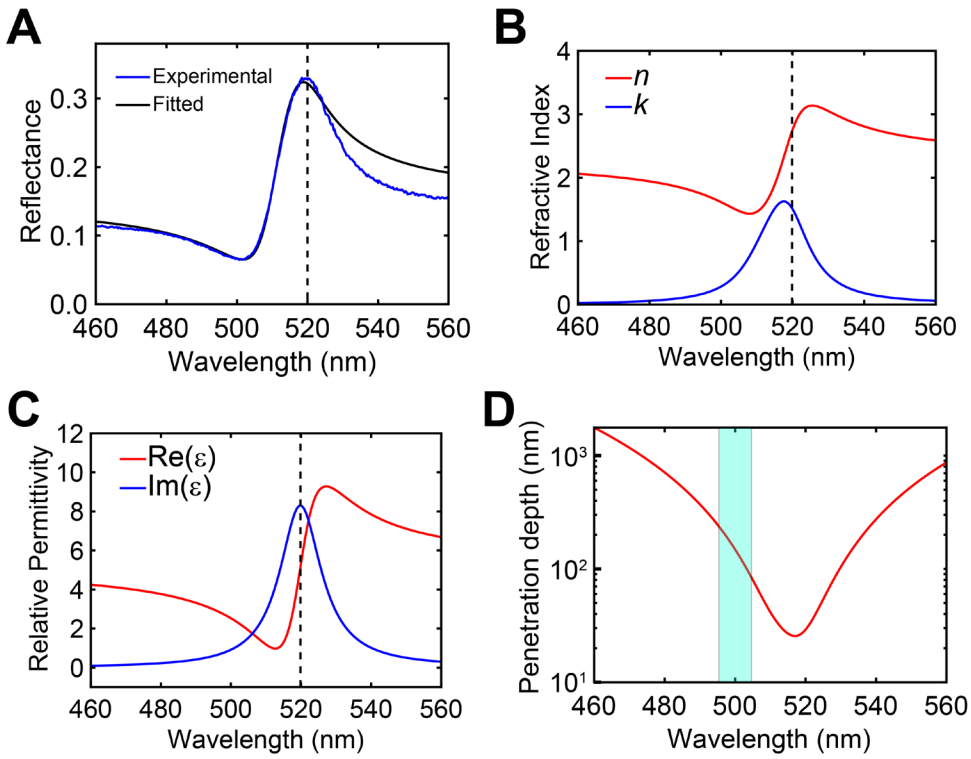

Figure S1. Fitting of the reflectance of PEA single crystal using the Lorentzian model. (**A**) Blue: reflectance spectrum of single-crystal PEA at room temperature. Black: calculated reflectance spectrum of PEA with the relative permittivity described by the Lorentzian oscillator $\varepsilon(\omega) = \varepsilon_\infty + \frac{{A_\mathrm{L}}^2}{{\omega_\mathrm{L}}^2 - \omega^2 - i\omega\gamma}$, where $\varepsilon_\infty = 5.07$ is the high-frequency permittivity, $\omega_\mathrm{L} = 2.39$ eV is the exciton energy, $\gamma = 67$ meV is the exciton damping factor, and $A_\mathrm{L} = 1.15$ eV is the oscillator strength. (**B**) Complex refractive index and (**C**) Complex relative permittivity of PEA calculated from the Lorentzian oscillator model. (**D**) Optical penetration depth, which is calculated as $1/\alpha$; α is the absorption coefficient determined as $\alpha = \frac{2\pi\varepsilon''}{n\lambda}$ (ε'' is the imaginary part of relative permittivity, n is the real part of refractive index, and λ is the wavelength). The optical penetration depth is equivalent to the depth at which the light intensity drops to $1/\mathrm{e}$ of the original intensity.

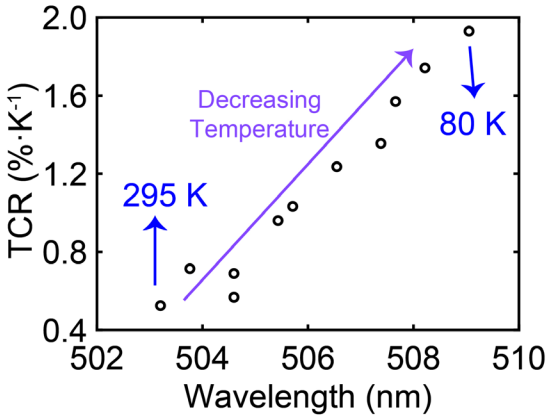

Figure S2. Temperature coefficient of reflectivity of PEA single crystal versus temperature. The *x*-axis represents the temperature-dependent wavelength at which single-crystal PEA exhibits the largest TCR. The *y*-axis shows the TCR values at the corresponding wavelengths.

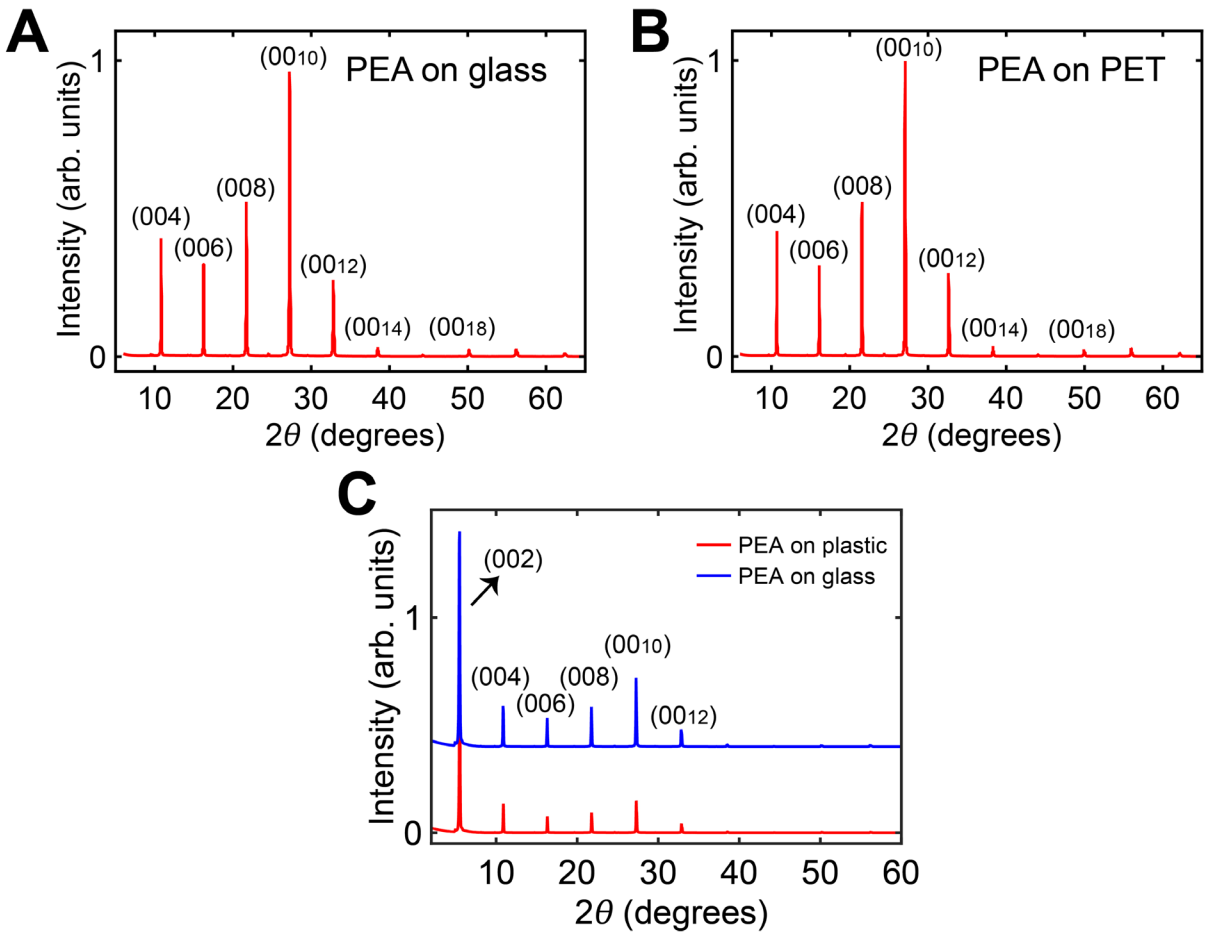

Figure S3. Structural characterization of PEA thin films. X-ray diffraction pattern of spin-coated PEA films on a glass substrate in (**A**) and on a PET substrate in (**B**). Data shown in (**C**) include the (002) peak between 2 to 10 degrees (the two curves are offset for clarity).

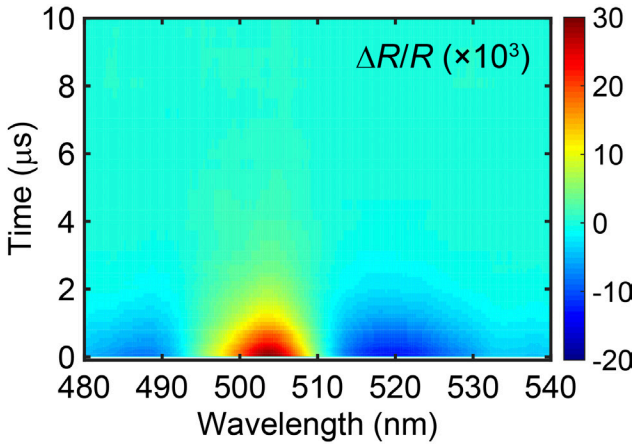

Figure S4. Transient spectral map of $\Delta R/R$ for 640 nm-thick spin-coated PEA film on Si measured at room temperature. The pump wavelength was 3170 nm and the pump fluence was 3.6 mJ·cm^{-2}.

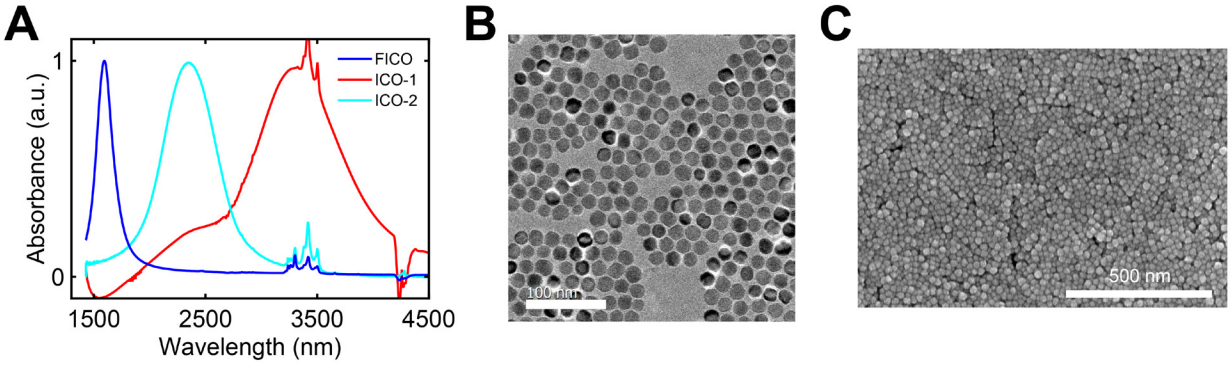

Figure S5. Optical and morphological characterization of the ICO nanocrystals. (**A**) Infrared absorbance spectra of the three types of ICO nanocrystals dispersed in toluene. (**B**) Transmission electron microscopy image of ICO-1 nanocrystals taken at 60,000X magnification, showing the uniform size distribution of the nanocrystals. (**C**) Scanning electron microscopy image showing the morphology of spin-coated ICO-1 nanocrystals on PEA/PET.

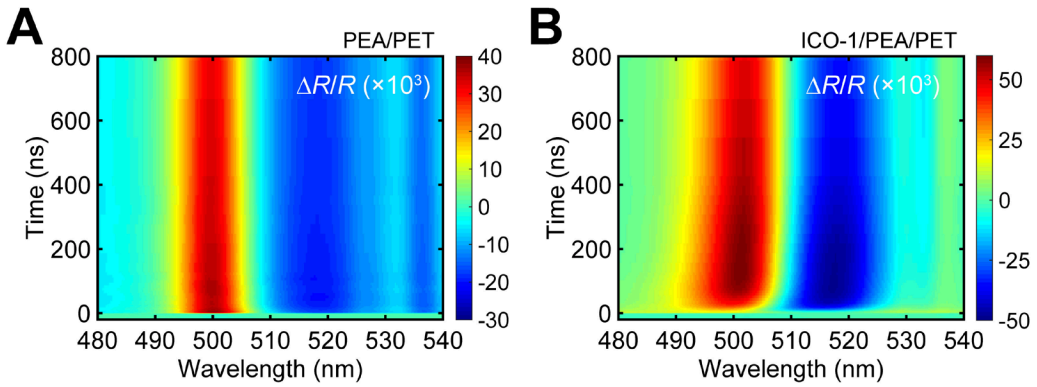

Figure S6. Transient optical response of PEA film without and with ICO nanocrystal coating. (**A**) Transient $\Delta R/R$ spectral map for a 940 nm-thick PEA film on PET measured at room temperature (pump wavelength: 3170 nm; fluence: 3.6 mJ·cm^{-2}). (**B**) Transient $\Delta R/R$ spectral map of ICO-1/PEA/PET at room temperature (pump wavelength: 3170 nm; fluence: 3.9 mJ·cm^{-2}).

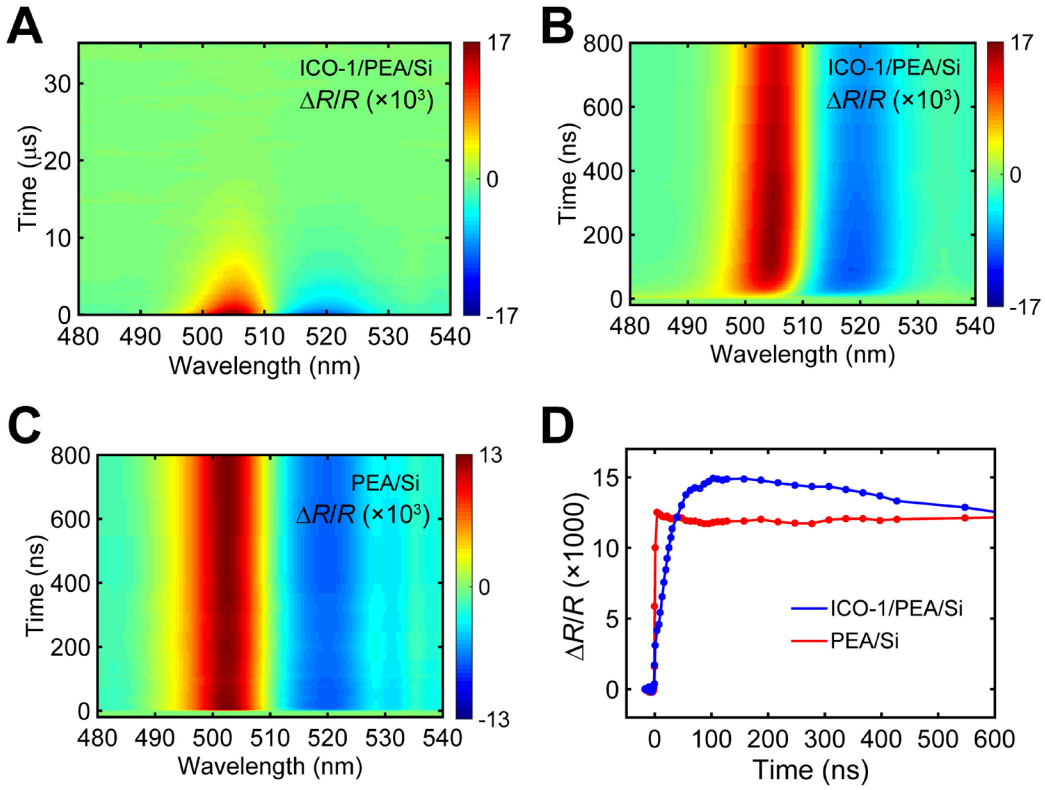

Figure S7. Transient optical response of PEA on silicon. (**A**) and (**B**) Transient $\Delta R/R$ spectral maps for ICO-1/PEA/Si measured at room temperature. (**C**) Transient $\Delta R/R$ spectral maps for PEA/Si measured at room temperature. (**D**) Comparison of the $\Delta R/R$ kinetics of the ICO-1/PEA/Si and the PEA/Si samples at 502 nm.

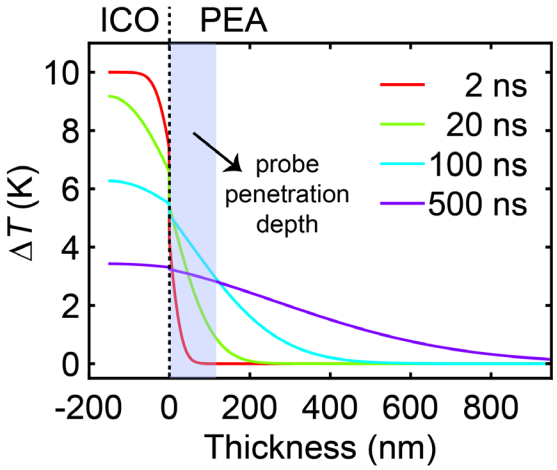

Figure S8. Simulated temperature profiles of ICO/PEA/PET. Simulated temperature profiles of an ICO/PEA/PET stack at various delay times following impulsive thermal excitation of the ICO film at time zero, showing energy transfer from ICO to PEA.

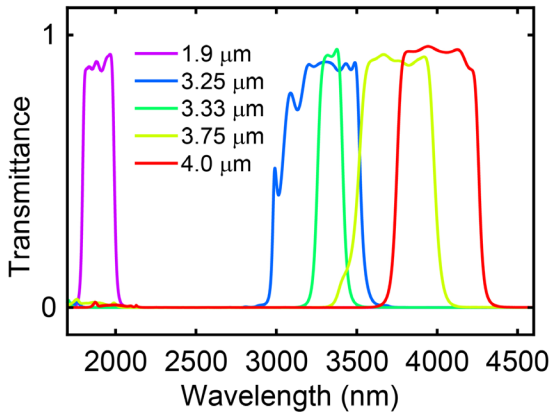

Figure S9. Transmittance spectra of the five MIR bandpass filters used in the MIR detection experiments. The transmittance curves are for FB1900-200, FB3250-500, FB3330-150, FB3750-500, and FB4000-500 filters (from short to long wavelength) measured with FTIR.

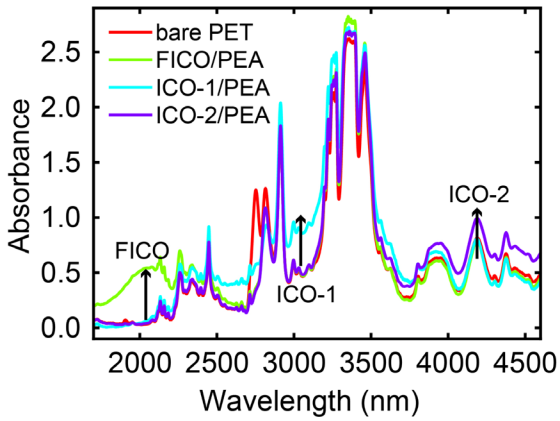

Figure S10. Infrared absorbance spectra for a bare PET substrate as well as PET substrates coated with PEA/Al_2O_3 and terminated with thin films of the three types of ICO nanocrystals. The enhanced absorption from the nanocrystal films is indicated by the black arrows in the figure. Note that the absorbance of MIR light by the PET substrate cannot be used to fulfill MIR photodetection function, because the absorption coefficient of MIR light for PET (0.5 mm thick) is much weaker than that for the ICO nanocrystals (<200 nm thick); only the ICO nanocrystal film can enable a heat concentrating effect for the PEA film.

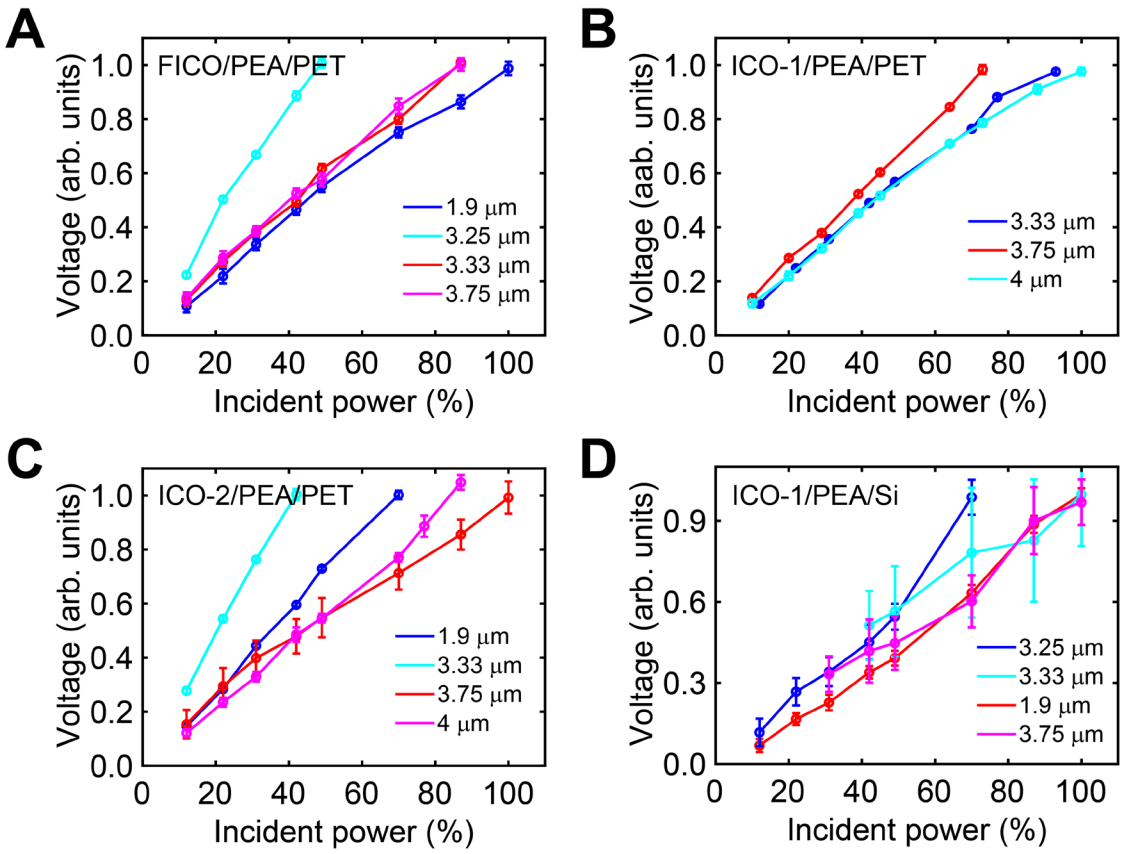

Figure S11. Tests of linear responsivity to the MIR power for the samples. Lock-in voltages measured as functions of the incident power of the MIR source used in the all-optical MIR detection experiments. Data for samples employing different ICO NCs are shown: FICO in (**A**), ICO-1 in (**B**), ICO-2 in (**C**), and ICO-1 with Si substrate in (**D**). Note that **1)** the magnitudes of MIR powers for different wavelengths are separately normalized, and **2)** the voltages measured with Si substrate in (**D**) have lower signal-to-noise ratios.

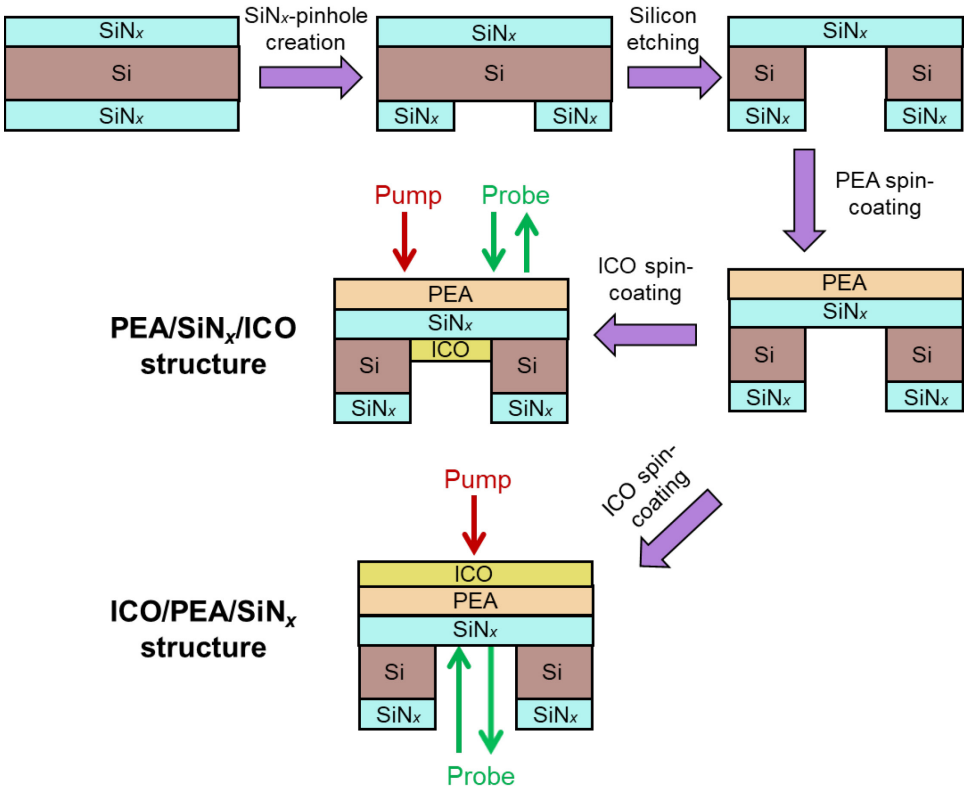

Figure S12. Schematic illustration for the fabrication procedure for the two types of membrane-based structures. Both the PEA/SiN_x/ICO used in Fig. 4 and ICO/PEA/SiN_x used in Fig. 5 are shown.

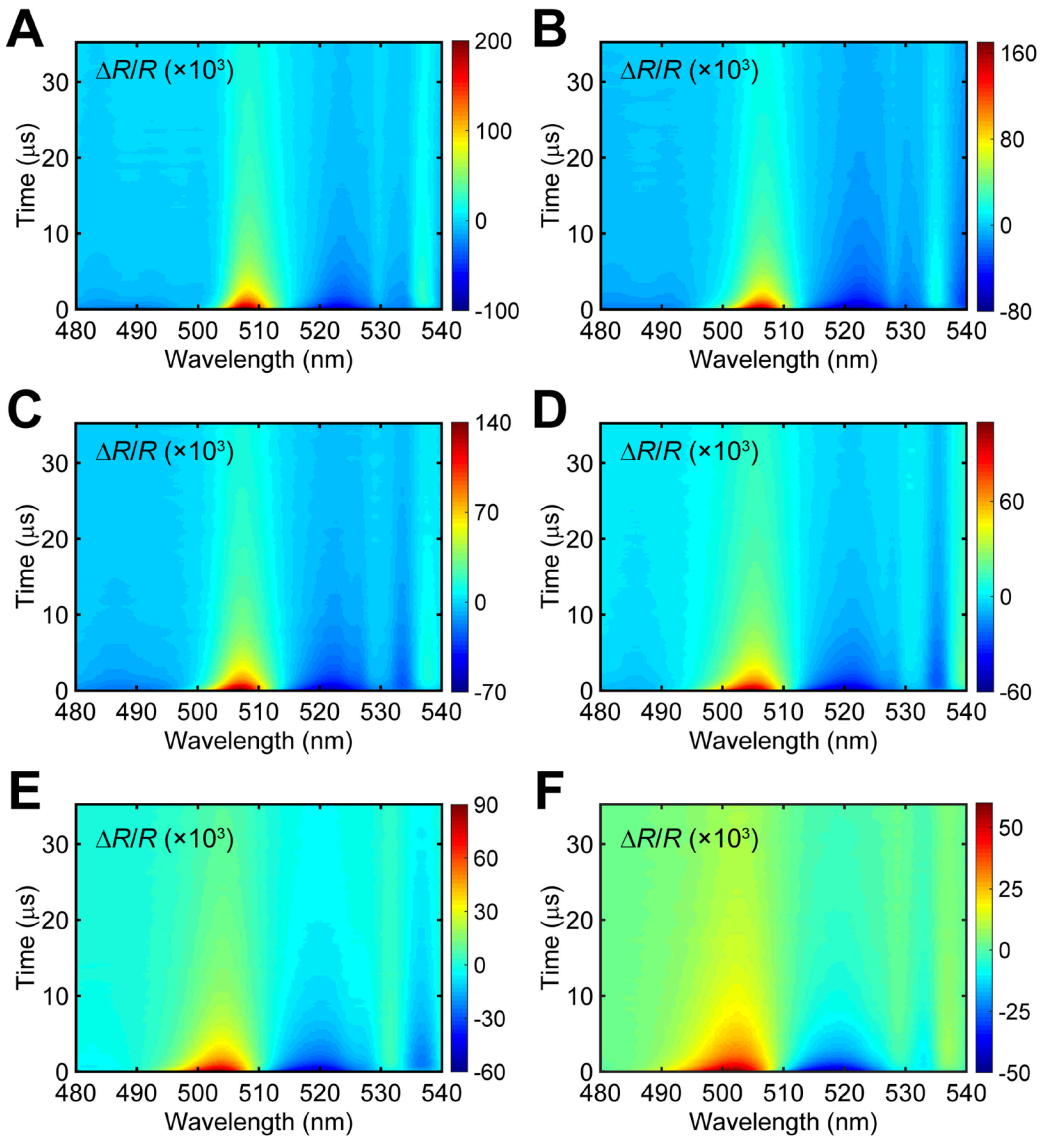

Figure S13. Temperature-dependent $\Delta R/R$ spectral maps. (**A**) to (**F**) Transient $\Delta R/R$ spectral maps for a single-crystal PEA measured at 80 K, 130 K, 170 K, 210 K, 250 K and 290 K, respectively (pump wavelength: 3170 nm; fluence: 2.3 mJ·cm^{-2}).

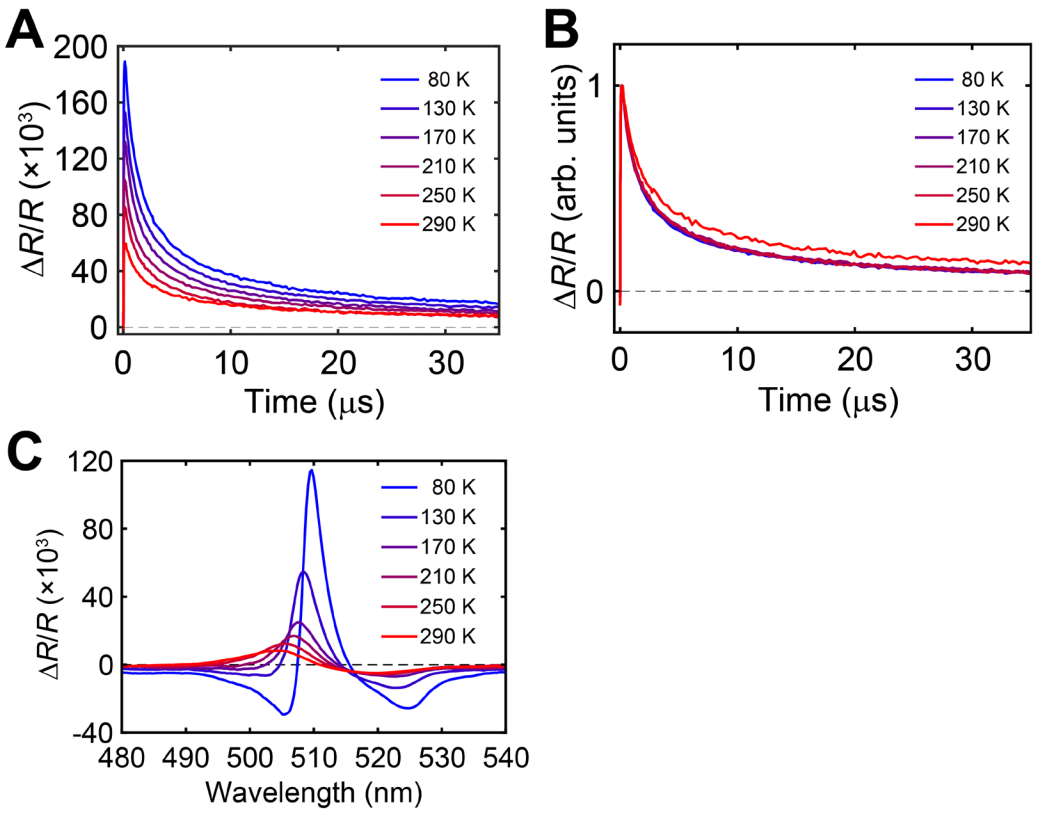

Figure S14. Temperature-dependent transient reflection measurements. (**A**) Temperature dependence of the $\Delta R/R$ kinetics measured for PEA/PET (thickness of PEA is 940 nm). The wavelength used in the plots is chosen to maximize the $\Delta R/R$ at each temperature. (**B**) Normalized plots of the data shown in (**A**). (**C**) Temperature-dependent $\Delta R/R$ spectra at 10 ns delay time for a PEA single crystal pumped at 3170 nm at fluence of 2.2 mJ·cm^{-2}.

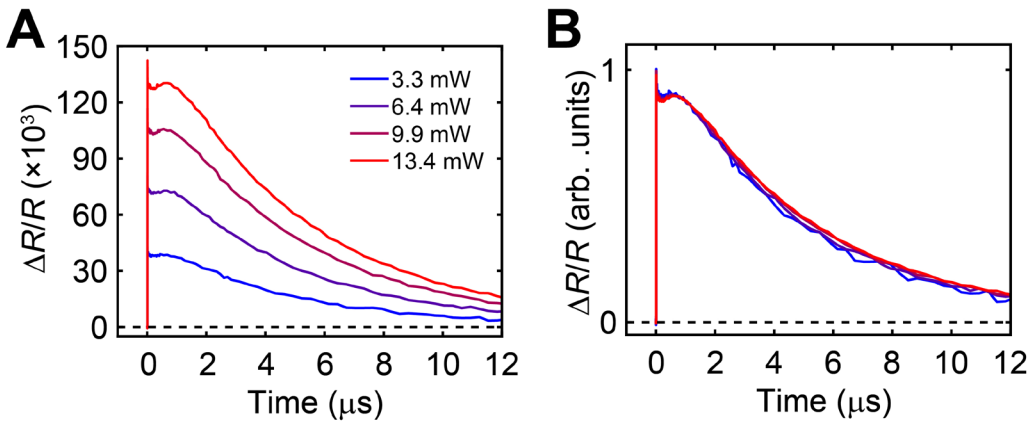

Figure S15. Pump power-dependent transient reflection measurements. (**A**) Pump fluence-dependent $\Delta R/R$ for a 640 nm-thick PEA on Si substrate measured at room temperature with (**A**) pump wavelength of 3170 nm. (**B**) Normalized version of the curves shown in (**A**).

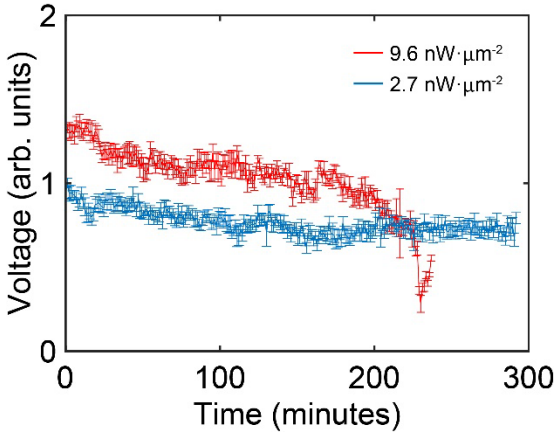

Figure S16. Stability tests. Stability test of SiN_x membrane-supported PEA film with its back side covered by a thin layer (<100 nm) of dielectric. The power densities indicated in the legend are calculated using the absorbed MIR powers by the sample, not the powers of incident MIR light.

Devices	Materials	Operation wavelength	Sensitivity	Temperature	Ref.
All-optical detection	$(PEA)_2PbI_4$	2-4.5 μm 10.6 μm	< 10 pW·μm^{-2} < 20 pW·μm^{-2}	Room temperature (RT)	This work
Nanoparticle-on-resonator	Au antenna and Biphenyl-4-thiol (BPT)	8.5-12.6 μm	1 μW·μm^{-2}	RT	[67]
Nano transducers	$NaYF_4:Nd^{3+}@NaYF_4$	4-11 μm	300 pW·μm^{-2}	RT	[12]
Charge density wave compound-based device	1T-TaS_2	visible to terahertz	(300 pW Hz$^{-1/2}$)	RT	[68]
Bolometer	Graphene	1.5 μm	(10 pW Hz$^{-1/2}$)	5 K	[69]
CMOS THz camera and polarimeter	CdSe/CdS/ZnS nanocrystals	0.1–1.5 THz	0.13 pW·μm^{-2} (**picosecond pulses** only)	RT	[70]
Microbolometer	Silicon nanomembrane	12.2 μm	115 nW·μm^{-2}	RT	[71]

Table S1. Comparison of different types of emerging schemes for long-wavelength light detection taken from various references.